SYNTHESIZING TITANIA BASED CATALYSTS FOR WATER SPLITTING AND CO_2 CONVERSION

A Thesis

by

REEM ABDELMONIEM ABDELAZIZ FARAJ

Submitted to the Graduate and Professional School of
Texas A&M University
in partial fulfillment of the requirements for the degree of

MASTER OF SCIENCE

Chair of Committee,	Nimir Elbashir
Committee Members,	Ahmed Abdala
	Bilal Mansoor
Head of Department,	Arul Jayaraman

August 2021

Major Subject: Chemical Engineering

ABSTRACT

Recently, blackening titanium dioxide has attracted attention as a promising catalyst for improving photoelectrochemical activity. It has been investigated for hydrogen production, and it is expected to have enhanced carbon dioxide conversion ability. In this study, a new generation of the titanium oxide catalysts referred to as the black titanium dioxide nanotube (BTNT) is tested to produce hydrogen from water splitting and carbon monoxide from carbon dioxide conversion. BTNT synthesis is optimized through electrochemical anodization and reduction in an ethylene glycol electrolyte. The synthesized material is also compared with the white titanium dioxide nanotube (TNT). The surface morphology, phase crystallinity, and oxidation states are confirmed by characterization using scanning electron microscopy (SEM), X-ray diffraction (XRD), and X-ray photoelectron spectroscopy (XPS). SEM shows a uniform nanotube structure with an average pore diameter of 65nm, while XRD indicated anatase crystallinity phase. The photoelectrochemical performance is investigated using the BTNT as a photoanode and a platinum wire as a cathode, where hydrogen was detected online via a residual gas analyzer (RGA). The highest performance is achieved in acidic conditions as the maximum percentage based on the gas sample volume reached 5.15% at an average current density of 1.75 mA/cm^2. BTNT is then tested in an electrochemical system to produce a mixture of CO/H_2 with a gold cathode. A qualitative model is developed for product analysis based on Fourier-Transform Infrared Spectroscopy (FTIR) and RGA for CO and H_2 detection, respectively. BTNT, compared to Pt, requires higher voltages to reach the same current densities and generate an equivalent amount of the product. The

final part of this work covers a detailed sustainability analysis of our developed system compared to other electrochemical and conventional CO/H_2 production routes. This analysis shows that the developed system needs to achieve higher CO_2 conversion to lower the CO_2 emissions and operating cost. Comparison with conventional routes showed that the electrochemical path needs further technological advancements that facilitates significant increase in energy efficiency such as lowering the overpotential, combined with substantial decrease in the renewable electricity price that could be achieved as well by new policies that provides incentives for this technology to be economically viable.

To my parents, who have always inspired me to believe in myself.

ACKNOWLEDGEMENTS

First, I would like to express my sincere gratitude to my advisor, Dr. Nimir Elbashir, for his support, critical insights on the work, and continuous encouragement. Also, I would like to thank my committee members Dr. Ahmed Abdala and Dr. Bilal Mansoor, for their guidance throughout this research.

I was fortunate to be part of Dr. Elbashir’s group, where I learned to engage in rich scientific discussions, which added to the work. I would like to thank every member for their insights and active guidance through my experimental research work. I am specifically grateful to Dr. Sun Hee Yoon, with whom I started this learning journey from zero experience. I am thankful to Mr. Anuj Parkash and Mr. Nasr Mohamed, who guided me patiently to learn about experimental work details. Mr. Anuj also closely helped me in the preparation of the Project Safety Analysis (PSA). I am indebted to Dr. Hanif Choudhury, who added to my practical skills and understanding of the work’s theoretical background. Moreover Dr. Mohamed Sufiyan Challiwala and Dr. Hanif assisted me in developing the work’s sustainability analysis. Besides, I would like to thank Dr. Yiming Wubulikasimu at the Central Materials Facility at TAMUQ for the time he devoted to training and helping me do multiple characterization tests. Special thanks to Dr. Anchu Ashok, who supported me at difficult times and never hesitated in giving me advice.

Many thanks to my friends, colleagues, department faculty, and staff who made my time at Texas A&M University a great experience. Finally, my deepest gratitude to my family for their encouragement, patience, and love.

CONTRIBUTORS AND FUNDING SOURCES

Contributors

This work was supervised by a thesis committee consisting of Dr. Nimir Elbashir and Dr. Ahmed Abdala from the Department of Chemical Engineering and Dr. Bilal Mansoor from the Department of Mechanical Engineering.

The experiments for hydrogen generation were done in Dr. Elbashir's lab at Texas A&M University in Qatar and with the help of Dr. Sun Hee Yoon, Mr. Anuj Varghese Prakash, and Mr. Nasr Mohamed. The experiments for the carbon dioxide conversion were done in Dr. Elbashir's lab with the help of Dr. Hanif Choudhury.

All other work conducted for the thesis was completed by the student independently.

Funding Sources

Graduate study was supported by a fellowship from Texas A&M University in Qatar. This work was also made possible in part by Qatar National Research Fund (QNRF) under National Priorities Research Program Grant Number [10-1210-160019]. Its contents are solely the responsibility of the authors and do not necessarily represent the official views of the Qatar National Research Fund (QNRF).

TABLE OF CONTENTS

Page

LIST OF FIGURES

LIST OF TABLES

Page

1. INTRODUCTION

In 2020, the global CO_2 emissions witnessed a decline of 5.8% due to the covid-19 pandemic, however the emissions from global energy-related activities sustained its level at 31.5 Gt (IEA, 2021a). This resulted in a record-high increase of 50% in the average annual concentration of atmospheric CO_2 compared to the industrial revolution's emissions level (IEA, 2021a). Furthermore, global CO_2 emissions is expected to bounce back by 4.8% by the end of 2021 as the normal life is resumed (IEA, 2021a). Carbon dioxide (CO_2) accounts for 65% of all greenhouse gas emissions, according to data reported by The Intergovernmental Panel on Climate Change (IPCC) (Ottmar et al., 2014). Substantial amounts of CO_2 are emitted from large industries such as natural gas processing, power generation, and iron and steel manufacturing (Ola et al., 2015).

To achieve the goal of lowering the global temperature by 2˚C in alignment with the Paris Agreement, IEA proposed a sustainable development scenario that requires 80% increase in the renewable energy capacity in all regions (IEA, 2021c). This scenario is complemented by nuclear energy and carbon capture and utilization technologies. These technologies will contribute to 15% of the reduction in cumulative CO_2 emissions (IEA, 2021b). Therefore, supporting this scenario encouraged extensive research activities for CO_2 utilization with an expected potential of 5 Gt/year consumption of CO_2 (Al Baroudi et al., 2021).

The growing efforts for climate change mitigation led to the creation of the CO_2 value chain. CO_2 can be used directly in enhanced oil recovery, stored in depleted oil and gas fields, or converted to feedstock and energy carriers. The CO_2 conversion can be achieved via different processes, including thermochemical (e.g., dry methane reforming), biological (e.g., algae for biofuels), electrochemical and photochemical processes (Jarvis & Samsatli, 2018).

Electrochemical CO_2 reduction has attracted attention due to the possibility of integration with a renewable source opening new venues for sustainable value-added products. Several advantages encourage the development of electrochemical CO_2 conversion, such as (a) allowing intermittent energy storage in chemical bonds, (b) maintaining a balance in the electric grid load to avoid supply and demand mismatch (c) providing as a modular system that not only allows on-demand manufacturing, but also practical and profitable system with limited capital investment, (d) possibility direct integration with the existing chemical infrastructure, (e) offsetting the costs of carbon capture while generating extra economic incentives, and (f) presents a highly tunable and environmentally benign process that operates under ambient conditions.

Electrochemical conversion of CO_2 gives a range of valuable products such as formic acid, carbon monoxide, methane, and alcohols (Hernández et al., 2017; Lee et al., 2019; Nguyen et al., 2020). The selectivity of a specific product depends upon several factors like catalyst choice, number of electrons, operating pressure, feed composition, operating temperatures, etc. (Mustafa, Lougou, Shuai, Wang, & Tan, 2020; Nguyen et al., 2020). Several recent literature reports have shown that carbon monoxide (CO) production via electrochemical conversion of CO_2 has the highest potential for approaching commercialization's benchmark targets.. However, to produce CO, usually high voltages are required, which incites hydrogen (H_2) evolution reaction from water splitting. This product mixture, CO and H_2, is known as synthesis gas (syngas), a versatile intermediate in the chemical industry. Syngas serves as a feedstock to many large-scale industries such as methanol production and synthetic fuels via the Fischer-Tropsch process (Abusrafa, Challiwala, Choudhury, Wilhite, & Elbashir, 2020; Abusrafa, Challiwala, Wilhite, & Elbashir, 2020; Alsuhaibani, Afzal, Challiwala, Elbashir, & El-Halwagi, 2020; Challiwala, Wilhite, Ghouri, & Elbashir, 2018; Hernández et al., 2017).

The sustainable production of syngas is relevant to four key markets natural gas monetization, transportation, energy storage, and petrochemicals. Such an opportunity is particularly of interest, where syngas infrastructure already exists. For example, the state of Qatar, which has the world's largest gas to liquid (GTL) plant and also the highest CO_2 in the world on a per capita basis, can integrate electrochemical CO_2 conversion with the existing facilities to reduce its CO_2 footprint (IEA, 2018). Currently, syngas is primarily produced from methane reforming via steam reforming or other technologies such as partial oxidation and auto-thermal reforming, all of which are energy-intensive processes (Pardal et al., 2017).

A typical electrochemical CO_2 conversion unit requires a cathode, an anode, an electrolyte, and a membrane separating the two electrodes. The membrane is used to prevent reoxidation of the products formed at the cathode, to facilitate separation of the gaseous products formed at the anode and cathode, and allow the use of different electrolytes in the cathode/anode compartments (Ramdin et al., 2019). CO_2 reduction happens at cathode surface, while oxidation reaction takes place at the anode. In producing syngas via electrochemical conversion, carbon monoxide from CO_2 reduction and hydrogen evolution from water are complementary, and both take place at cathode surface. The most selective metal cathode materials for carbon monoxide production are silver and gold (Hernández et al., 2017). Gold electrocatalysts can achieve high current densities at lower overpotentials as compared with silver. In a study by Verma et al., a gold catalyst was shown to achieve 99 mA/cm^2 with an energy efficiency of 64% (Sumit Verma et al., 2018). Higher current densities were reached in systems using silver electrodes, consequently requiring higher overpotentials, which results in lower energy conversion efficiency (45 to 50%) (Dufek, Lister, Stone, & McIlwain, 2012; Ma et al., 2016).

Many studies in electrochemical CO_2 reduction are directed towards the development of cathode materials. However, a recent study shows that the cathode material is not the bottleneck of CO_2 electrolyzer feasibility. Electrolyzer's cost breakdown indicates that 61.2% against 3.7% goes to the anode vs. cathode electrocatalysts (Masel et al., 2021). That is because the limiting reaction is the oxygen evolution taking place at the anode surface, which requires higher voltage and four electrons to give one oxygen molecule (Z. Sun et al., 2017). Regarding operating cost, the main contributor is electricity from the renewable source (Adnan et al., 2020). Therefore, photoelectrochemical routes may reduce electricity costs by directly utilizing sunlight while being more efficient than the photochemical process. The main challenge for efficient photoelectrochemical CO_2 reduction systems is to find an appropriate semiconductor material acting as a highly active photoelectrode. Among the various kinds of developed semiconductor candidates, titanium dioxide (TiO_2), with a combination of desirable properties including good chemical stability, nontoxicity, low cost, and most importantly, suitable band energy levels for the desired water splitting and CO_2 reduction reactions, is an ideal model of semiconductor photoelectrode to investigate (Ma et al., 2014). Using TiO_2 as a photoanode with electrocatalysts such as Cu_2O can achieve high selectivity to carbonaceous products with low bias (Chang et al., 2016).

In considering the electrochemical syngas production process, two pathways can be identified direct syngas production in a single step and dual step process. In dual step process, CO and H_2 are produced independently then mixed to the targeted ratio. An emerging aspect is the efficacy comparison between the mentioned two processes. Jouny et al. suggested that the dual-step process of syngas production is more economically favorable because higher selectivity reduces the total electricity needed (Jouny, Luc, & Jiao, 2018). Another techno-economic study that defines performance parameters' values to attain profitability compared direct and dual-step processes based on the relationship between the syngas ratio and the maximum operating voltage for economic feasibility (S Verma, Kim, Jhong, Ma, & Kenis, 2016). Their results suggest that the operating voltage needs to be below 2.25V for the syngas ratio (1:1) to be profitable compared to 3.5V for only carbon monoxide production. In other words, direct syngas production can be profitable under certain conditions. Speaking of the technical feasibility of achieving different syngas ratios from single-step production, a study by Dioxide Materials and 3M companies investigated routes for tuning the syngas ratio between 1 and 4, including pH controlling or using a bimetallic cathode material, i.e., silver/nickel (Liu et al., 2016).

This research discusses two elements, (a) the experiments for exploring black titanium dioxide and its application in water splitting and carbon dioxide conversion; (b) the scalability of the developed syngas electrochemical production based on economic and environmental analysis. Therefore, in the next section, relevant literature review about electrochemistry principles, developments in anode materials, and process sustainability are detailed.

2. LITERATURE REVIEW

2.1. Electrochemistry Background

Electrocatalysis is the catalysis branch, which involves oxidation/reduction reactions occurring at the electrode-electrolyte interface (Léger et al., 2007). The process requires an electrocatalyst to lower the reaction overpotential (similar to the activation energy barrier in conventional catalysis) (Léger et al., 2007). Electrocatalysis requires two electrodes: the cathode where the reduction reaction occurs, i.e., the process of gaining electrons, and the anode where the oxidation reaction occurs, i.e., the process of losing electrons (Skoog et al., 2018). Photocatalysis can be considered a branch of electrocatalysis since it also involves oxidation/reduction reactions, but both happen at the photocatalyst's surface (R. Li et al., 2017). Photochemical reactions are driven by light absorption, which creates electron/hole pairs to perform the reduction/oxidation reactions, respectively (R. Li et al., 2017). Photosynthesis is an example of a photocatalytic process where the plants can convert carbon dioxide and water to valuable products using sunlight. However, as photocatalytic processes are slow with low conversion efficiencies limited by light absorption, a combination of photo- and electrochemical pathways emerged as photoelectrochemical processes. A photoelectrochemical process is where a photocatalyst is used as an anode or cathode in an electrochemical cell. This section will review some electrochemistry fundamentals followed by a discussion of carbon dioxide reduction and water splitting as examples of electrochemical and photoelectrochemical processes.

An electrochemical cell is used to test electrocatalysts for the conversion of electricity to chemical energy. Cell potential (E_{cell}) is the difference in potential between the two half-reactions, i.e., oxidation and reduction, that give the complete reaction(Skoog et al., 2018). It is related to the change in free energy through the following equation:

$\Delta G = -nFE_{cell}$…...……………………… [2-1]

F is the Faraday constant (96,485 coulombs per mole electron), and n is the number of moles of electrons associated with the oxidation/reduction process (Skoog et al., 2018). At equilibrium, ΔG° is related to the standard cell potential, E°_{cell}, which can be calculated via redox tables for half-reactions potentials at standard conditions (Skoog et al., 2018). In the energy applications, Table 1 presents the standard cell potential for selected reactions.

Table 1: Equilibrium potentials for selected energy related reactions (Hori, 2008)

Reaction	E°cell vs RHE (V)
$2H^{+} + 2e^{-} \rightarrow H_2$	0
$CO_2 + 2H^{+} + 2e^{-} \rightarrow CO + H_2O$	-0.11
$CO_2 + 6H^{+} + 6e^{-} \rightarrow CH_3OH + H_2O$	0.02
$2CO_2 + 12H^{+} + 12e^{-} \rightarrow C_2H_5OH + 3H_2O$	0.08
$2H_2O \rightarrow O_2 + 4H^{+} + 4e^{-}$	1.23

The values presented in this table are based on the thermodynamics of the reactions; however, the actual cell potential (E_{cell}) is higher due to the electron transfer to activate the reactants, mass transport limitations, surface conversions, or ohmic losses from electrode/electrolyte conductivity (Carmo et al., 2019). Thus, the term overpotential, η, which is defined as the difference between the equilibrium potential and experimentally observed potential:

$\eta = E_{cell} - E^{\circ}_{cell}$…….……………………… [2-2]

Electrochemical reactions are studied in a three-electrode system: working electrode, a counter electrode, reference electrode in an electrolyte connected to a potentiostat/galvanostat device as shown in Figure 1 (Skoog et al., 2018). The working electrode is the examined material where the reaction of interest occurs while the counter electrode is to complete the circuit. A reference electrode is an electrode with a known potential independent of the ions involved in the reaction and is necessary to measure the working electrode potential (Skoog et al., 2018).

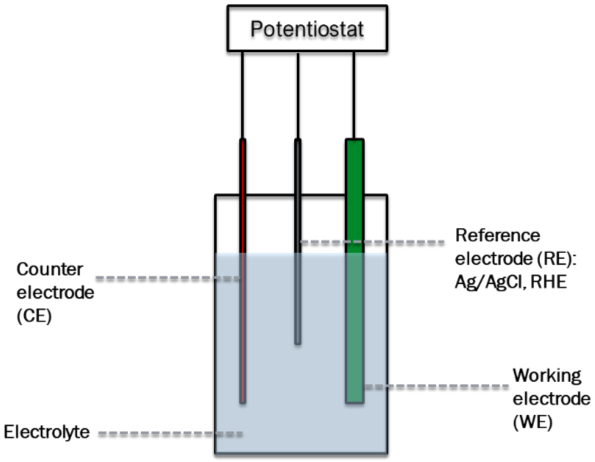

Figure 1: Electrochemical cell schematic

An example of an electrochemical process is the reduction of carbon dioxide to carbon monoxide. A typical electrochemical CO_2 conversion unit, as shown in Figure 2 requires a cathode, an anode, an electrolyte, and a membrane separating the two electrodes. The membrane's function is to block the transfer of redox reactants/products and allow only ions' movement to close the circuit. The CO_2 reduction takes place at the cathode surface, while the oxidation reaction occurs at the anode. Since the media is aqueous, H_2

evolution will also happen at the cathode surface. The reactions in the system are as follows:

At the anode, H_2O electrolysis takes place:

$2\mathrm{H_2O} \rightarrow \mathrm{O_2} + 4\mathrm{H}^+ + 4e^-$…...……………………………. [2-3]

At the cathode, two reactions take place:

$\mathrm{CO_2} + 2\mathrm{H}^+ + 2e^- \rightarrow \mathrm{CO} + \mathrm{H_2O}$…...……………………..... [2-4]

$2\mathrm{H}^+ + 2e^- \rightarrow \mathrm{H_2}$…...……………………………………. [2-5]

∴The overall reaction:

$\mathrm{CO_2} + \mathrm{H_2O} \rightarrow \mathrm{CO} + \mathrm{O_2} + \mathrm{H_2}$…...………………………... [2-6]

The most demanding step is the activation energy required for the electron transfer to the CO_2 molecule to form the radical $CO_2^{\cdot -}$ as follows:

$\mathrm{CO_2} + e^- \rightarrow CO_2^{\cdot -}$ …...……………………………………. [2-7]

This reaction has a Gibbs free energy (ΔG°) of 183.32 kJ/mol compared to 19.9 kJ/mol for CO in reaction [2-6].

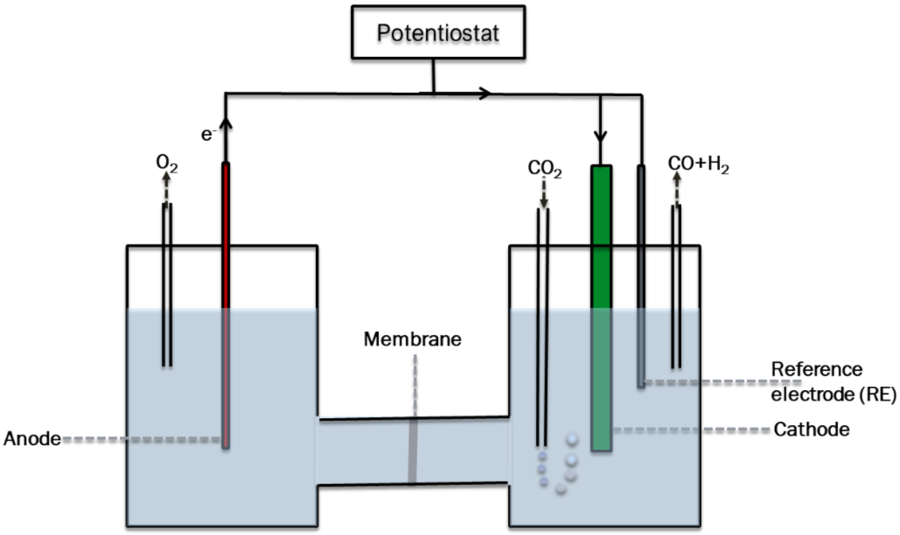

Figure 2: Components of a two compartments electrochemical cell

A photoelectrochemical cell is also a three-electrode system, typically a one compartment cell as shown in Figure 1, where the working electrode is a semiconductor. The difference is that a solar simulator is used to irradiate the semiconductor while it is connected to the potentiostat. The photoelectrochemical water splitting to produce H_2 and oxygen, involves three main steps (Iqbal et al., 2018):

1. Photoanode absorbs sunlight to generate electron-hole pairs,
2. Photo-induced holes at photoanode surface cause water oxidation, releasing oxygen,
3. Photo-induced electrons travel through the external wire to the cathode, where the reduction reaction releases H_2 gas

The voltage supply is required for efficient electron/hole separation and accelerating the reaction kinetics (Joy et al., 2018). The reactions for water splitting are summarized below (Iqbal et al., 2018):

The reactions at the photoanode:

$2hv + semiconductor \rightarrow 2\mathrm{h}^+ + 2\mathrm{e}^-$…..………….. [2-8]

$\mathrm{H_2O} + 2\mathrm{h}^+ \rightarrow \frac{1}{2}\mathrm{O_2} + 2\mathrm{H}^+$…...……………………… [2-9]

The reaction at the cathode:

$2\mathrm{H}^+ + 2\mathrm{e}^- \rightarrow \mathrm{H_2}$ …………………………………... [2-10]

Net reaction:

$\mathrm{H_2O} \rightarrow \mathrm{H_2} + \frac{1}{2}\mathrm{O_2}$ …………………………………… [2-11]

Where, 'h' stands for the Planck constant (6.626×10^{-34} J·s), 'v' is the frequency of illuminated photons, 'h^+' and 'e^-' are the holes and electrons photogenerated from the semiconductor, respectively. For the photoanode to be activated by sunlight, it must have energy higher than the bandgap. The bandgap is the energy difference between the conduction and valence band (Tentu et al., 2017). The energetic photons excite the valence band's electrons to jump to the conduction band leaving behind the holes (Ahmed et al., 2019). The electrons transport to the electrode/electrolyte interface from which they can flow to the cathode through the external wire (Ahmed et al., 2019). Therefore, it can be concluded that the smaller the bandgap, the lower energy needed to activate electron/hole pairs.

2.2. Photo-electrochemical Materials

Photo-electrochemical materials are semiconductors that are used as photoelectrodes in a photoelectrochemical (light-assisted electrochemical) system. The photoelectrochemical performance depends on having appropriate bandgap and band edges, good optical properties, low recombination rates of photogenerated holes and electrons, good electrical conductivity, and sufficient stability (Ahmed et al., 2019; Ismail et al., 2014). Photoelectrodes include metal oxides, transition metal nitrides or sulfides, and carbon-based materials (Yao et al., 2018). The metal oxide, titanium dioxide (TiO_2), is the most studied photocatalyst where researchers are trying to increase its activity and enhance the light absorption properties through bandgap engineering (Z. Zhang et al., 2013). Zinc oxide (ZnO) is another metal oxide widely studied and has a similar bandgap to TiO_2, limiting its light absorption. Carbon-based materials such as composites loaded with graphene oxide are recently studied because of the excellent electron mobility and large surface area, promoting the suppression of charge recombination(Joy et al., 2018).

2.2.1. Development in TiO_2 and black TiO_2

Fujishima and Honda were the first to use titanium dioxide (TiO_2) for water splitting (Fujishima et al., 1972). TiO_2 has been extensively studied because it has several desired properties, including availability, ease of preparation and modification of electronic structure, high charge carriers mobility, high refractive index, good oxidizing ability besides long term stability, and low cost (de Brito et al., 2018; Naldoni et al., 2019; Tentu et al., 2017). TiO_2 has three types of crystal phases, tetragonal rutile, tetragonal anatase, and orthorhombic brookite (Ismail et al., 2014; White et al., 2015). The difference in crystal structure affects the electronic properties such as charge transfer and band energy levels (Shen et al., 2018). Anatase and rutile are the most studied phases for photoelectrochemical applications. Anatase is generally more active due to higher charge mobility and longer exciton diffusion length (Luttrell et al., 2014).

However, TiO_2 has two main challenges, the wide bandgap and the fast recombination reactions (X. Kang et al., 2019; Naldoni et al., 2019). The bandgap width limits the TiO_2 optical absorption to the ultraviolet (UV) region, which is only 5% of the solar spectra (B. Wang et al., 2017). Enhancement of TiO_2 performance can be via engineering the bandgap through different methods such as doping with metals (Ganesh et al., 2014), self-doping (Zhu et al., 2018), plasmonic enhancement (Z. Wang et al., 2013a), or incorporation of charge separating scaffolds (Ahmed et al., 2019). Recombination reactions of photoinduced holes and electrons can be slowed down by modifying the nanostructure of TiO_2 (Ismail et al., 2014). Materials with smaller particle sizes inhibit the recombination probability of photogenerated electrons and holes on their surface, thereby facilitating their smooth transport (Ullattil et al., 2018). Moreover, nanoparticles possess a high surface area availing more active sites on the surface.

Recent studies have focused on reducing TiO_2 surface to fabricate black TiO_2. This method of surface disordering leads to extended visible light absorption and efficient spatial separation of electron-hole pairs(Shen et al., 2018). The black coloration is related to the presence of $Ti^{3+,}$ which may occur due to oxygen vacancies following reduction (Ullattil et al., 2018). These oxygen vacancies contribute to enhancements in electrical conductivity and charge transportation(Q. Kang et al., 2013). The conduction band minimum of the black TiO_2 nanoparticles is thermodynamically and kinetically favorable for water and CO_2 reduction (Ullattil et al., 2018). Wang et al. reduced titanium dioxide by aluminum at 500˚C and could boost photocatalytic H_2 production 8.5 times higher than pristine TiO_2 (Z. Wang et al., 2013b). Xu et al. used an electrochemical reduction approach for obtaining black TiO_2 nanotubes, which showed enhanced photoactivity and a photocurrent density of 0.65 mA/cm^2 at 0 V vs. Ag/AgCl (C. Xu et al., 2013). Jeong et al. used a two-step anodization process to obtain TiO_2 nanotubes transplanted onto fluorine-doped SnO_2 substrates. The prepared black TiO_2 nanotubes could achieve an eight-fold higher photocurrent and accelerated oxygen evolution reaction (Jeong et al., 2018). A combination of electrochemical reduction and nitrogen doping was attempted by Yu et al. and observed a decrease in the band gap from 3.2 eV to 2.0 eV (Yu et al., 2018). Reduced TiO_2 nanotubes were also used for photocatalytic CO_2 reduction by Gao et al. where they could produce CO at a rate of 185.39 μmol/g h (Gao et al., 2020).

In this study, we employ electrochemical anodization and reduction to obtain black TiO_2 nanotubes. These two approaches were chosen for their easiness, low cost, benign conditions with potential scalability.

2.2.1.1. Fabrication of nanotubular structure

For semiconductors to harvest sunlight efficiently, maximizing specific surface area is crucial (Joy et al., 2018; X. Yan et al., 2017). Nanostructures have been explored to allow more active sites and also to slow down the recombination reactions of electrons and holes, facilitate charge transport, and improve the reaction kinetics by altering electronic properties (Roy et al., 2011; Ullattil et al., 2018; X. Yan et al., 2017).

The different dimensions of nanostructures can enhance certain properties; for instance, 0D (e.g., quantum dots) are known for high visible light absorption, 2D (e.g., nanosheets) absorbs more UV light due to its small thickness, while 3D exhibits high photoactivity (Joy et al., 2018). Nonetheless, 1D nanostructures such as nanotubes and nanorods are the most attractive for water splitting applications (Roy et al., 2011). The interest in 1D nanostructures especially nanotubes is because they provide a higher surface area, lower the recombination rate, and enhance the redox reaction rate due to unidirectional electron transport (Cho et al., 2014; Venturini et al., 2019; Xuemei Zhou, 2017).

To fabricate nanotubes, various methods have been studied where the oldest method first reported by Hoyer is electrochemical deposition (Hoyer, 1996). Another technique developed by Kasuga et al. (1998) is based on the hydro/solvothermal approach. Other methods aerosol–gel (Zhang et al., 2001), atomic layer deposition (Shin et al., 2004), and electrochemical processes. The most used method is electrochemical anodization since it results in a highly uniform and closely packed nanotube structure with the advantage of controllable tube length (Roy et al., 2011). The electrochemical anodization method is facile and benign in ambient conditions, and its potential scalability allows the nanotubes to grow directly perpendicular to the conductive metal surface (Roy et al., 2011).

Zwilling et al. (1999) are the first to report nanotube synthesis using electrochemical anodization, highlighting the fluoride ions' role. To obtain uniformly organized nanotubes, organic electrolyte systems (e.g., ethylene glycol) are ideal and can yield micrometer-length nanotubes (Roy et al., 2011). In the electrochemical anodization process, the morphology of TiO_2 can be tuned by adjusting process parameters (e.g., potential, pH, anodization time, and solution concentration) or by adding some specific species to the electrolyte (Shah et al., 2017). The properties and concentration of ionic and nonionic species (organic) in the electrolyte are the main factors for the effective growth and formation of nanotubes (Shah et al., 2017).

The anodization mechanism explained in the previous studies (Dikova et al., 2014; Shah et al., 2017; Smith et al., 2013; Y. Sun et al., 2011) begins with a field-assisted oxidation reaction in which oxygen ions dissolved in water react with Titanium to form an oxide layer according to the equation below (Sun, Wang, & Yan, 2011):

$\mathrm{Ti} + 2\mathrm{H_2O} \rightarrow \mathrm{TiO_2} + 4\mathrm{H^+} + 4\mathrm{e^-}$ …………………………………… [2-12]

However, another competitive reaction is taking place in the field-assisted dissolution reaction due to the fluoride ions. The fluoride ions dissolve the titanium dioxide and form a complex ion (TiF_6) in the equation below (Sun et al., 2011):

$TiO_2 + 6F^- + 4H^+ \rightarrow [TiF_6]^{2-} + 2H_2O$……………………………… [2-13]

The dissolution reaction breaks through the oxide layer, develops into a hole, and eventually grows to form a nanotubular structure (Dikova et al., 2014).

2.2.1.2. Blackening Effect

Blackening of the TiO_2 can be achieved in various ways. The most employed method is hydrogenation of TiO_2, where Chen et al. (2011) converted white TiO_2 to black at 200 °C under 20.0 bar H_2 pressure in 5 days (Xiaobo et al., 2011). Blackening occurs due to introducing oxygen vacancies or Ti^{3+} into the TiO_2 lattice (B. Wang et al., 2017). Other methods include H_2 plasma treatment (Z. Wang et al., 2013a), chemical oxidation (Liu et al., 2013), reduction by metals such as aluminum (Z. Wang et al., 2013b), zinc (Z. Zhao et al., 2014), or magnesium (Sinhamahapatra et al., 2015) and electrochemical reduction (H. Li et al., 2014).

The blackening mechanism involves field-assisted intercalation/extraction of monovalent cations, which modify the bandgap's electronic states (Zheng et al., 2014). During the reaction, H_2 is produced and diffused to react with the oxide layer (Wu et al., 2014). As it gets ionized to H^+, an electron is delocalized in the conduction band, reducing Ti^{4+} to Ti^{3+} and oxygen vacancies (Wu et al., 2014). The reduction reaction equation is given by (Wu et al., 2014):

$Ti^{4+}O_2 + e^- + H^+ \rightarrow Ti^{3+}(O)(OH)$ ……………………………… [2-14]

The oxygen vacancies are oxygen defects in the TiO_2 lattice that can either be active sites or recombination centers (Amano et al., 2016).

2.3. Sustainability of the Process

CO_2 utilization is one way to mitigate climate change while producing economically viable products. Qatar, with the highest per capita emissions, aspires to new technologies to reduce these emissions. The country needs a compatible solution to benefit from the existing gas-to-liquid infrastructure (GTL). Globally, renewable electricity prices are decreasing as the technology is maturing and more capacity is installed. In line with the global efforts, Qatar is pursuing a plan towards more sustainable electricity production as it aims for 20% of its energy from solar power by 2030. In July 2020, Siraj-1, the first large-scale solar power project with 800MW output, was announced and expected to achieve full capacity by 2022 (TOTAL, 2020). Qatar General Electricity & Water Corporation signed a power purchase agreement with the project company at one of the lowest equivalent Levelized Electricity Cost (LEC) of 0.01567$/kWh (Keating, 2020). Therefore, electrochemical CO_2 conversion to syngas coupled with renewable electricity could be a suitable route to reduce CO_2 emissions while benefiting from the existing GTL infrastructure.

Recently, there have been efforts by big companies to commercialize electrochemical CO_2 technologies. For example, Siemens has collaborated with Covestro and Evonik and developed a low-temperature electrolyzer for syngas production. This unique electrolyzer system demonstrates an industrially relevant current density of 300 mA/cm^2 (Haas et al., 2018). Following this advance, testing is being conducted on a pilot-scale plant, with an ultimate goal of integration with GTL plants by 2030 (Kuhn, 2020). Another example is the low-temperature CO_2 electrolyzers developed by Dioxide Materials company based on innovative membranes that can reach up to 500 mA/cm^2 at 3V with 95% selectivity to carbon monoxide (Dioxide Materials, 2018). For the high-temperature processes, Haldor Topsoe offers a full-scale solid-oxide electrolysis cell that produces a high purity carbon monoxide (99.999%), with an energy efficiency of 45% (Haldor Topsoe, 2019).

CO_2 is stable thermodynamically, marking its reduction as an energy-intensive process. For example, CO_2 to CO needs ca. 18.4 GJ/ton CO with 50% conversion efficiency is very close to steel production energy requirement (ca. 21GJ/ton) (Grim et al., 2020). Thus, to evaluate the benefits of electrochemical CO_2 conversion, calculating the CO_2 footprint and net fixation is required. Several recent studies focused on the techno-economic assessment of the different products from electrochemical CO_2 conversion (Adnan et al., 2020; De Luna et al., 2019; Jarvis et al., 2018; Jouny et al., 2018; Nabil et al., 2021; Verma et al., 2016). These studies concluded that CO is the closest to economic viability, and the critical bottleneck for this process is the electricity price.

This study focuses on comparing electrochemical syngas production models starting from the developed experimental setup. The sustainability analysis is based on environmental and economic metrics to compare with the pilot and commercial systems reported in the literature. The expected outcome is to shed light on the direction of the work progressing in electrochemical CO_2 conversion to syngas and how it stands compared to off-field benchmark CO_2 conversion technologies.

3. RESEARCH PROBLEM AND OBJECTIVES

3.1. Research Problem

Recently black TiO_2 has been studied for H_2 generation and has proven higher efficiency than white TiO_2. Few studies on the photocatalytic CO_2 reduction on black TiO_2 are found in the literature. However, it can be seen from the literature survey that black TiO_2 is not fully explored in electrochemical CO_2 conversion. Studies are needed to investigate the catalytic ability of black TiO_2 to drive CO_2 electrochemical conversion and analyze the possible products. Such investigation will give insight into the potential of this material to substitute the expensive noble metal in photo/electrochemical CO_2 conversion systems.

Furthermore, the potential of the scalability and commercialization for the electrochemical-based processes for CO_2 conversion still required tremendous research and development efforts. A detailed sustainability assessments methods and tools are required to ensure the emerging of new catalysts and technologies in this market.

3.2. Research Objectives

This study focuses on using black TiO_2 nanotubes (BTNT) for producing H_2 and converting CO_2 to CO in a photo/electrochemical cell.

The systematic approach to achieve this goal is as follows:

1. Synthesis of the black TiO_2 uniform structured nanotubes.
2. Characterization of the BTNT.

3. Study of the photo/electrochemical properties using electrochemical measurement techniques.
4. Building an electrochemical setup that allows direct analysis of gaseous products and safe operation.
5. Performance testing the BTNT for H_2 generation.
6. Comparison of the BTNT with white TiO_2 nanotubes based on surface characterization, electrochemical properties and H_2 generation.
7. Validation of the built setup for CO_2 conversion using standard material of platinum.
8. Performance testing the BTNT for CO_2 conversion.
9. Preliminary economic and environmental analysis of the developed system based on CO_2 emissions and operating cost. The obtained results are compared with literature reported electrochemical systems.
10. A sensitivity study to highlight the impact of the system's specifications on the CO_2 emissions and cost.

4. METHODOLOGY

This section consists of two parts; the first part discusses the experimental approach used for the fabrication and characterization of the BTNT, then the techniques for analyzing its electrochemical properties and the performance tests for production of H_2 and conversion of CO_2. The second part elaborates the calculation steps for CO_2 emissions and operating cost of the proposed electrochemical process for syngas production. The CO_2 emissions and the operating cost are used to assess the sustainability of the process and compare it with literature reported systems.

4.1. Experimental Methods

4.1.1. Materials and Chemicals

Titanium (thickness 1mm, 99.7% trace metals basis, Sigma-Aldrich) and stainless steel (thickness 1.5mm, Sigma-Aldrich), gold (thickness 0.1mm, 99.99%, Shanghai Yue Magnetic Electronic Technology Co., Ltd.,) and platinum (thickness 0.1mm, 99.99%, Shanghai AI FA Technology Co., Ltd.) are cleaned and used as detailed. Chemicals' sources and purities are as follows, ethylene glycol ($C_2H_6O_2$) (≥98%, VWR Chemicals), sodium fluoride (≥99%, Sigma Aldrich), potassium bicarbonate (99.97% trace metals basis, Sigma Aldrich), potassium hydroxide (KOH) (≥99%, Sigma Aldrich), nitric acid (69%, VWR Chemicals) and sulfuric acid (>95%, Fisher Scientific). Deionized water (≥18.2 MΩ, TOC ≈ 1ppb, Purelab Flex from Elga) is used to prepare all solutions. The following gases are used for purging, CO_2 (99.995%, grade 4.5, NIGP) and N_2 (99.9995%, grade 5.5, NIGP).

4.1.2. Fabrication Procedures

This section elaborates on the fabrication of the titanium dioxide nanotubes (TNT) and the black titanium dioxide nanotube (BTNT). The chosen procedures are based on electrochemical processes, as explained in the introduction section. The parameters of the experiments were based on both literature and optimization experiments which are discussed in detail in Appendix A. Figure 3 summarizes the discussed fabrication steps of the BTNT electrode.

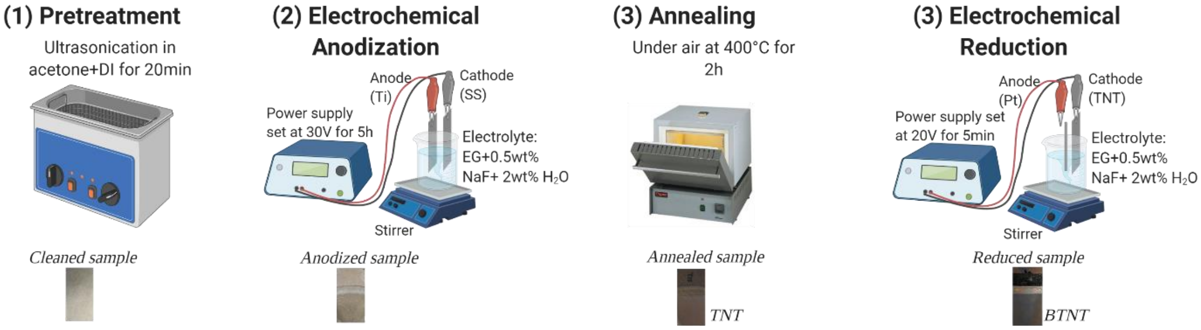

Figure 3: Overview of BTNT fabrication (created with biorender.com)

4.1.2.1. Titanium Dioxide Nanotubes (TNT) Preparation

Titanium (Ti) sheet (2cm x 4cm x1mm in size) and stainless-steel (SS) sheet were cleaned in acetone and deionized water under ultrasonication (Branson 2510E) for 10min then dried in ambient air. The Ti sheet as anode and stainless-steel as cathode were immersed vertically in an ethylene glycol electrolyte solution containing 0.5wt % NaF and 2wt % H_2O (Jeong et al., 2018). A constant voltage of 30V was provided by the power supply (Quad Output DC, EXTECH Instruments; max. 60V) for 5h at room temperature and stirring speed of 4rpm. The experimental setup as in the lab is shown in Figure 4. The as-anodized titanium was then washed with deionized water and left to dry in ambient conditions before annealing at 400˚C for 2h in a muffle furnace (Thermolyne, Thermo Scientific). The resulting sample is referred to as TNT. The conditions used in the electrochemical anodization and the annealing resulted from optimization experiments explained in Appendix A.

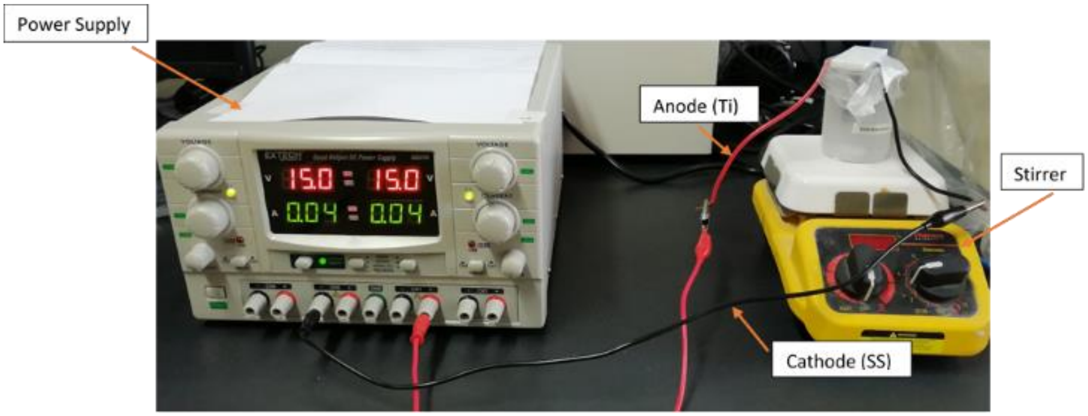

Figure 4. Electrochemical Anodization Setup

4.1.2.2. Black TNT Preparation

Electrochemical reduction reaction was conducted using the same power supply at a constant potential of 20V and for 5min. As shown in Figure 5, the TNT was set as the cathode against a Pt wire as the anode in the same electrolyte solution of ethylene glycol (0.5wt % NaF and 2wt % H_2O) stirred at 4rpm and ambient conditions. It is worth mentioning that using a higher voltage (i.e.,>20V) for reduction caused peeling of the TNT's oxide layer.

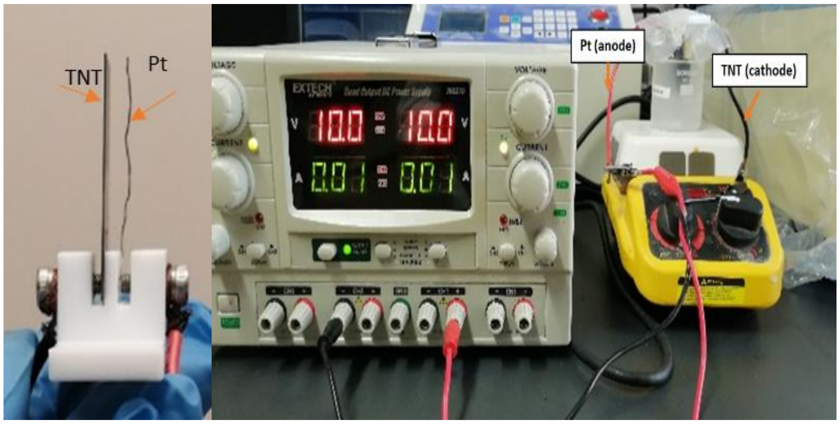

Figure 5: Electrochemical Reduction Setup

4.1.3. Materials Characterization Methods

4.1.3.1. Scanning electron microscopy (SEM)

Scanning electron microscopy (SEM) is a versatile instrument primarily used to analyze the topology and morphology by imaging a surface with a focused electron beam (Akhtar et al., 2018). Topology provides information about the surface texture, while morphology indicates shape and size. SEM is highly advantageous to get high-resolution images up to 1nm (Akhtar et al., 2018). In this study, SEM from FEI QUANTA 400, Thermo Fisher Scientific operated at a vacuum of 10Pa, and an acceleration voltage of 5kV is used to confirm the surface morphology of TNT and BTNT.

4.1.3.2. X-ray diffraction (XRD)

X-ray diffraction (XRD) is a non-destructive technique used to characterize crystallographic structures, phases, chemical composition, and other details (Bunaciu et al., 2015). XRD generates peaks by constructive interference of monochromatic beam of X-rays that creates diffracted ray through interaction with the sample (Bunaciu et al., 2015). The diffracted ray is scattered at certain angles from each lattice plane of the sample. Since each material has a distinctive X-ray diffraction pattern for its atomic arrangement, this pattern can be compared with reference measurements to identify the crystalline form (Bunaciu et al., 2015). In this study, XRD is recorded by a Rigaku Ultima IV diffractometer using Cu (Kα) radiation (40 kV/40 mA) to characterize the crystalline structure and compare TNT with BTNT. Bragg's law is used to identify crystal type via the following relation (Skoog et al., 2018):

$n \cdot \lambda = 2d\sin\Theta$ ………………………………………. [4-1]

where, 'n' is an integer, 'λ' is the X-ray wavelength, 'd' is the crystal interplanar distance, and 'θ' is the beam angle. Matching 2θ versus the X-ray intensity with the diffraction pattern is used for the identification of the crystalline phase.

4.1.3.3. X-ray photoelectron spectroscope (XPS)

X-ray photoelectron spectroscope (XPS) is a non-destructive instrument used for quantitative chemical analysis, e.g., total elemental analysis and chemical bonding details (Andrade, 1985). It uses the photoelectric effect concept where X-ray source emitting monochromatic X-ray photons interact with the atomic and molecular orbital electrons in the sample (Andrade, 1985). A fraction of the photoelectrons emitted from 1-10 nm of the surface is analyzed to measure the kinetic energies (Andrade, 1985). Thus, a spectrum of photoelectron intensity versus the binding energy is generated where the binding energy position of the characteristic peaks is used for elemental identification (Andrade, 1985). The oxidation states of Ti and O in both TNT and BTNT were examined using XPS (AXIS Ultra DLD X-ray Photoelectron Spectrometer by Kratos (UK).

4.1.4. Electrochemical Measurement Techniques

The Interface 1010E potentiostat/galvanostat from Gamry instruments was used to conduct cyclic and linear sweep voltammetry besides chronoamperometry. The potentiostat is an electronic instrument used to control and measure voltage or current between the working and reference electrode (Westbroek, 2005). It is used to study reaction mechanisms related to reduction/oxidation chemistry (Westbroek, 2005). This device interfaces with a computer and has a dedicated software package from which different experiments can be chosen, e.g., voltammetry (cyclic or linear) and chronoamperometry (Westbroek, 2005). A typical system is the three-electrode which has a working, counter, and reference electrodes. The device controls the potential between the working and reference by adjusting the current through the counter electrode (Skoog et al., 2018). Chronoamperometry is an electrochemical technique that monitors the current versus time at the fixed potential to the working electrode (Ciobanu et al., 2007). Voltammetry is an electroanalytical method which plots current against the potential of the working electrode(Ciobanu et al., 2007).

4.1.4.1. Cyclic Voltammetry (CV)

Cyclic Voltammetry (CV) is an electrochemical technique used to find the reduction/oxidation (redox) potentials, the thermodynamics, and the effect of media on redox reactions (Elgrishi et al., 2017). A three-electrode cell is connected to a potentiostat which sweeps the voltage with a specific scan rate while measuring the current (Elgrishi et al., 2017). The voltage sweeps proceed in cycles where the positive voltage ramp provides the oxidation peak and vice versa for the reduction peak (Elgrishi et al., 2017).

In this study, CV was used to evaluate the oxidation potentials of the prepared BTNT in the range from -1.2 to 1 V at a scan rate of 100 mV/s.

4.1.4.2. Linear Sweep Voltammetry (LSV)

Linear Sweep Voltammetry (LSV) is used to determine the onset potential and the samples' photocurrent density. As the applied voltage approaches the redox potential, the current increases (Brian, 2013). The electrons' movement in and out the electrode due to the redox reactions causes the current to measure the rate of the exchanged electron at the electrode-electrolyte interface (Brian, 2013). Herein, the potential values were swept in the range from -0.5 to 1.5V vs. Ag/AgCl reference electrode at a scan rate of 5 mV/s under chopped light irradiation (100 mW/cm^2) using a 150 W xenon arc lamp (ABET LS150).

4.1.5. Analytical Equipment

4.1.5.1. Residual Gas Analyzer (RGA)

RGA is a spectrometer that measures gasses' chemical composition at vacuum conditions (Ohring, 2002). RGA is considered convenient because of its simple operation and instantaneous measurement. In this device, injected gas molecules are converted to ions then filtered according to their specific mass to charge ratio (M/e) (Ohring, 2002). The mass to charge ratio and the signal response measurement are related to the number of injected molecules. Two main limitations of RGA operation are faced in this study: (1) the nitrogen and carbon monoxide overlapping peaks since both have an atomic mass unit of 28 and (2) the mass spectrum of the CO_2 has a fragment of CO of about 12% intensity

(Timo et al., 2006). Therefore, in this work, the RGA from Hiden Analytical was used to detect only the H_2 generation.

4.1.5.2. Fourier-Transform Infrared Radiation Spectroscopy (FTIR)

FTIR is a method that identifies chemical bonds via their vibration (bending or stretching) when exposed to infrared radiation at specific wavelengths (Daéid, 2005). The vibration intensity against the radiation frequency is plotted, and a portion of the spectrum is signified as the fingerprint region, which is unique to each functional group (Daéid, 2005). In this study, FTIR from NICOLET 670, Thermo SCIENTIFIC was used to identify the C≡O bond, typically found in the range (2200-2100cm^{-1}), as shown in the below figure obtained from NIST (Acree et al.). FTIR is chosen as it is recommended for small samples and can detect CO as low as 1ppbv (Novelli, 1999).

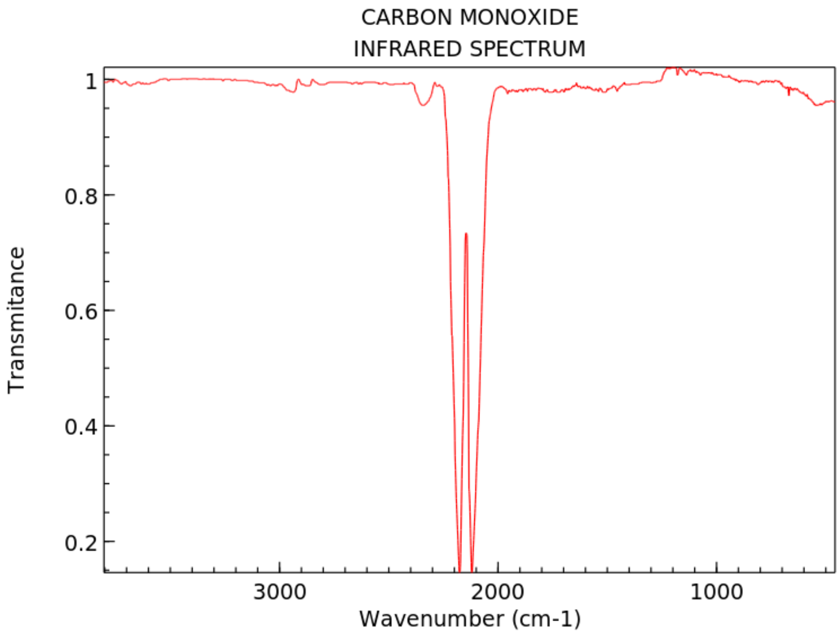

Figure 6: Infrared spectrum of carbon monoxide (Acree et al.)

4.1.6. Water Splitting Setup

Figure 7 shows a schematic of the experimental setup, and Figure 8 shows the layout as in the lab. A customized quartz glass cell was used for the two-electrode system comprising TNT or black TNT as working electrodes, while the Pt wire was the counter electrode. Three types of electrolytes, KOH (1M), H_2SO_4 (0.5M), or mixture, were used to investigate the effect of pH. The potentiostat supplied the setup with the voltage and measured the current density over the reaction time. The cell was under air mass 1.5 (AM1.5) irradiation (100 mW/cm^2). The solar simulator was warmed up for 10 minutes before each experiment to avoid irradiation instabilities. H_2 rate was measured using the RGA connected to the cell's headspace - that records all exit gas signals instantly.

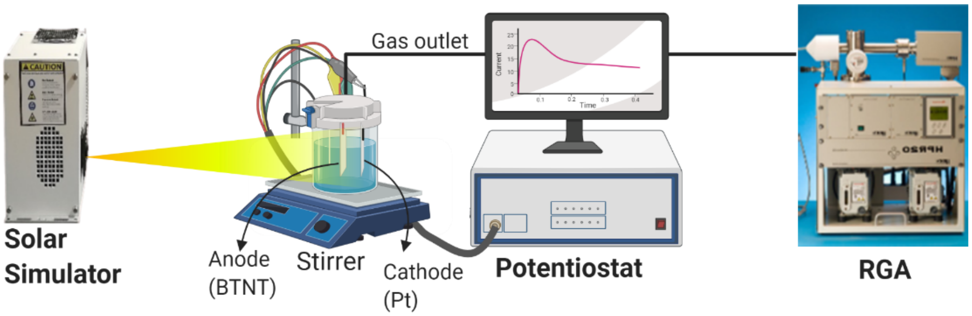

Figure 7: Schematic of the experimental setup for H_2 generation under AM1.5 irradiation (100 mW/cm^2)

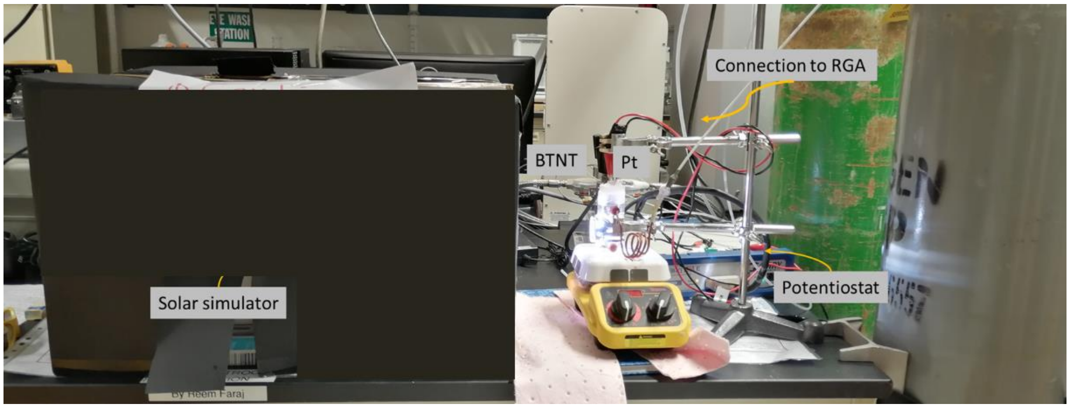

Figure 8: Experimental setup for H_2 generation as in the lab

4.1.7. CO_2 Conversion Setup

The BTNT testing for the CO_2 conversion was conducted in a typical two-compartment (H-cell) electrolysis cell obtained from Mi Hua Agel Ecommerce Ltd. The two compartments were separated by an ion-exchange membrane (Nafion, 117), stored overnight in 0.1M $KHCO_3$ before use (Cave et al., 2017). Since this reaction is sensitive to impurities, a cleaning and pretreatment protocol was followed before each experiment (Cave et al., 2017; J. Zhao et al., 2020). Firstly, the cell was cleaned using 40 vol% sulfuric acid and rinsed with DI water. A gold plate was used as the cathode and BTNT or platinum (for the validation and comparison) as the anode. The gold plate was polished with sandpaper, ultrasonicated in a 40 vol% aqueous nitric acid solution, then in DI water and ethanol for 15 minutes to remove contaminants. The platinum plate was cleaned in 40 vol% nitric acid overnight, then ultrasonicated and rinsed with DI water and ethanol, whereas the BTNT was used as it is. To set up the cell, each compartment was filled with 60 ml of 0.1M $KHCO_3$ solution. A chiller maintained the cell at a fixed temperature of 20˚C. Low temperatures enhance the CO_2 solubility in the electrolyte (Gattrell et al., 2006). An Ag/AgCl reference electrode was used and placed in the cathodic compartment. The data was recorded versus an Ag/AgCl electrode and shifted to the RHE scale using Nernst equation (Ciobanu et al., 2007):

$$\mathrm{E_{RHE}} = \mathrm{E_{Ag/AgCl}} + 0.059\ \mathrm{pH} + \mathrm{E^{\circ}_{Ag/AgCl}} \ldots\ldots \quad [4\text{-}2]$$

Where $E^{\circ}_{Ag/AgCl} = 0.21V$

The cathodic compartment was purged with N_2 first for at least 15 minutes, then three cyclic voltammograms (CV) were taken. All three CVs were in the range of -1.2 V to 2.3 V vs. RHE, where the first and third runs at a low scan rate of 50mV/s and the second run at a high scan rate of 500mV/s. The idea behind several cycles at different scan rates is to stabilize the surface by getting rid of any impurities and ensuring the surface was free of any poisoning electroactive species (Cave et al., 2017). Then, the cathodic compartment was purged with CO_2 for 15 minutes, and the cyclic voltammograms were repeated. Subsequently, an anodic pretreatment step was done by fixing the potential at 2.3V for 30 minutes. This anodic voltage of 2.3V is based on a previous study that relates the formation of a gold oxide layer to an increase in the surface area (Hoogvliet et al., 2000).

The electrolyte's pH measurement in the cell was done before and after CO_2 purging, and the readings were recorded, respectively. The pH values were used to ensure the electrolyte saturation with CO_2 (J. Zhao et al., 2020). For product detection, the analytical equipment was connected to the headspace of the cathodic compartment. Figure 9 is the schematic of the described electrochemical setup. The qualitative assessment of the evolving gaseous products was conducted by FTIR for CO detection and RGA for the detection of H_2. Before each experiment, the analytical equipment was purged with the carrier or inert gas for around one hour to ensure the system is free of contaminants. The RGA records all gas signals instantly and represents the data as partial pressure or ppm. In the FTIR, the measurements were taken every five minutes, and the carrier gas was 10% CO_2 in helium. In all experiments, the flow of carrier gas through the cell was regulated with a rotameter (Cole Parmer) at 120 ml/min to ensure the relatively high flowrate will prevent air from entering the cell.

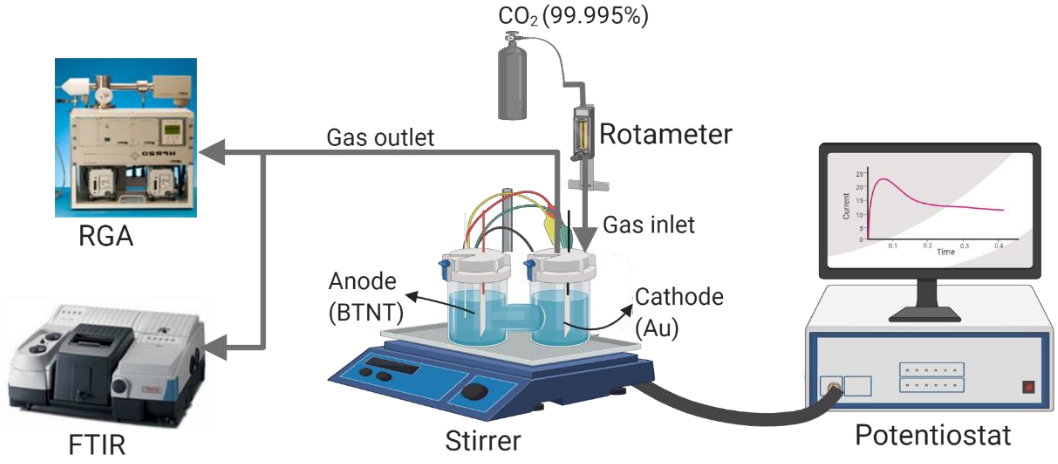

Figure 9: Schematic of CO_2 electrochemical reduction setup. The cell is connected to a potentiostat, a rotameter regulates the CO_2 inlet, and the RGA/FTIR analyzes the gas outlet (created with BioRender.com)

Chronoamperometry experiment was used by specifying the voltage and time. Different voltages versus RHE were explored: -0.40, -0.7, -1V; these values are based on the CO_2 reduction window (-0.4 to -1V) (Goyal et al., 2020). Each experiment was repeated at least three times for 30 minutes with continuous stirring of the electrolyte.

4.2. Environmental and Economic Analysis

In this section, the CO_2 emissions and the operating cost for the tested experimental setup are evaluated and compared with the literature-reported pilot/commercial systems and conventional syngas benchmark. The literature-reported pilot/commercial cases are from Siemens and Dioxide Materials companies. The conventional syngas benchmark is taken as dry methane reforming since it also converts CO_2 to syngas. Analysis of the electrochemical systems requires the calculation of electricity, energy efficiency, and conversion, which are calculated through the equations provided below. Per Faraday's law, the maximum CO generated can be calculated using the equation below (Skoog et al., 2018):

$$N\left(\frac{mol}{s}\right) = \frac{J\times A\times 10^{-3}}{n\times F} \ldots\ldots\ldots\ldots\ldots\ldots\ldots\ldots\ldots\ldots\ldots \text{[4-3]}$$

where, 'J' is the current density (mA/cm^2), 'A' is the electrode area in cm^2, 'n' is the number of electrons involved in the reaction (for CO=2), and 'F' is the Faraday's constant (96,485 C/mol).

It should be noted that equation [3-2] can also be used for scaling up the experimental setup by substituting the value of 'N' in the equation with the targeted production capacity of syngas.

The electricity consumption can be calculated as follows:

$$E = \frac{V\times J\times A\times t}{EE\%} \ldots\ldots\ldots\ldots\ldots\ldots\ldots\ldots\ldots\ldots\ldots\ldots\ldots \text{[4-4]}$$

where, 'V' is the applied voltage (volts), 't' is the operating time (s), and '$EE\%$' is the energy efficiency which is calculated as follows(De Luna et al., 2019):

$EE\% = \frac{E^{\circ}}{V} \times 100\%$ …………………………………… [4-5]

where, 'E°' is the equilibrium cell potential calculated from the following equation (Skoog et al., 2018)::

$E^{\circ} = E_{cathode}{}^{\circ} - E_{anode}{}^{\circ}$ ……………………………[4-6]

For electrochemical syngas production, two pathways were considered as shown in Figure 10; (a) direct syngas production, and (b) dual-step process. Scenario (a) uses one electrolyzer to convert CO_2 and H_2O streams to syngas at the specified ratio. This scenario is studied by two cases: the experimental setup and Siemens reported syngas electrolyzer. On the other hand, scenario (b) uses two electrolyzers: one to convert CO_2 to CO and the other to produce H_2 from H_2O. This scenario is studied by the commercial CO electrolyzer developed by Dioxide Materials company coupled with a commercial H_2 electrolyzer. A solar energy source and pure CO_2 stream are assumed available on-site. Table 2 summarizes the specifications of the four analyzed cases.

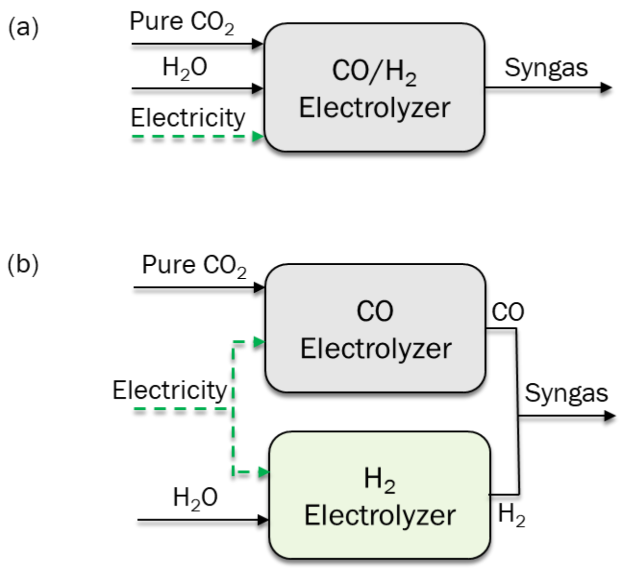

Figure 10: Electrochemical syngas production pathways via (a) direct reduction of CO_2 to syngas, (b) dual step process to convert CO_2 and H_2O to syngas where electricity is assumed from solar panels.

Table 2:Specifications of the studied systems

		Typical Examples		
Parameter	Current study	Siemens	Dioxide Materials	H_2 from AEM
Current density (mA/cm^2)	4.14	150.00	120.00	300.00
Cell potential (V)	2.23	3.60	2.95	2.10
FE%	50%	47%	98%	100%
Reference	This work	(Haas et al., 2018)	(Kaczur et al., 2018)	(Carmo et al., 2013)

In an electrochemical system, CO_2 emissions are generated from indirect emissions associated with the manufacturing, construction, and commissioning of solar panels and CO_2 stream purification. The electrochemical system's cost is broken down into a capital cost which includes electrolyzer, and an operating cost which includes CO_2 stream and renewable electricity.

Table **3** summarizes emissions factors and unit prices used for CO_2 emissions and costs.

Table 3: Emission factors and unit prices

Emissions factors		**Reference**
Solar Panel (utility) (gCO_2/kWh)	48	(Bruckner et al., 2014)
CO_2 stream (gCO_2/kg CO_2)	62.95	(David et al., 2001)
Economics		
Price of CO_2 (\$/kg)	0.03	(Luckow et al., 2015)
Electrolyser Cost (\$/kW)	300	(DOE, 2015)
Electrolyser Cost (\$/m^2)	1840	(Jouny et al., 2018)

4.2.1. Calculation Method

As shown in Figure 11, the steps for CO_2 emissions calculation start by assuming a production basis which is taken as 1000 kg CO/day. Also, the targeted ratio is set as (H_2:CO = 1:1), which corresponds to a faradaic efficiency of 50%. This faradaic efficiency falls almost in the middle of the literature-reported values range (20 to 90%) based on CO (Cave et al., 2017; Ringe et al., 2020). Required electrolyzer area and electricity demand can be calculated from equations [3-3] and [3-4]. Electricity consumption by the supporting components or systems (balance of plant) is assumed as 10% of the electricity demand in the conversion process (Adnan et al., 2020). From CO_2 reduction reaction stoichiometry and conversion percentage, CO_2 demand can be calculated. Finally, emissions are calculated by multiplying electricity and CO_2 stream by emission factors and subtracting the quantity of CO_2 converted to CO. The operating cost (OPEX) is comprised of CO_2 stream and electricity. Detailed calculations and assumptions are provided in Appendix A.

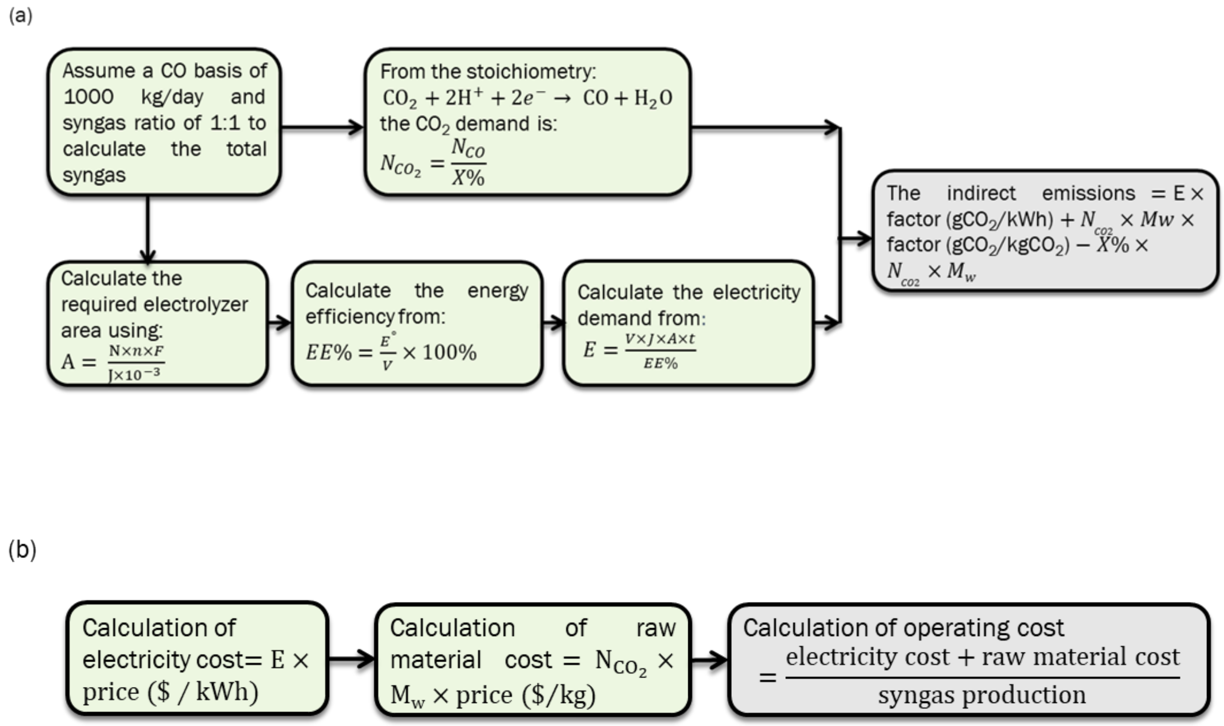

Figure 11: Steps for the calculation of the (a) CO_2 emissions and (b) the operating cost

5. RESULTS AND DISCUSSION

Herein, the discussion starts by the experimental results followed by the environmental and economic analysis. The discussion of the experimental work starts by the material characterization for comparing morphology, crystalline structure, and oxidation states between the BTNT and the TNT. Afterwards, the electrochemical measurements to investigate electronic conductivity and reduction/oxidation potentials are elaborated. Lastly, the performance of the material in H_2 production and CO_2 conversion is discussed. In the second part, the CO_2 emissions, and costs for scaling up the proposed electrochemical syngas process are discussed. Additionally, a comparative analysis is demonstrated with similar and conventional benchmark syngas production processes. The discussion is concluded by a sensitivity study to highlight the bottleneck of the process.

5.1. Experimental Results

5.1.1. Surface Characterization

5.1.1.1. SEM

Surface structure and dimensions can be tuned by varying the applied voltage and duration of the anodization reaction. As the nanotube length increases, it allows more area for light absorption enhancing the catalytic ability of the material (Adán et al., 2016; Y. Sun et al., 2011; Z. Wang et al., 2013a; Xuemei Zhou, 2017). However, after a length greater than ∼7−10μm, the probability for recombination increases which lowers the photoactivity (Adán et al., 2016; Z. Wang et al., 2013a; Xuemei Zhou, 2017). The nanotube surface is the main reaction place thus bigger pore diameter and small thickness are preferred to enhance ion migration (Liang et al., 2012). Through tuning the anodization parameters, the desired nanotubular structure with a pore diameter average of 65 nm and a length between 4 to 6μm was obtained, as depicted by the SEM surface and the cross-section images in Figure 12 and Figure 13. The SEM revealed that both TNT and BTNT have similar morphology indicating that the electrochemical reduction does not change the nanotube structure formed in the anodization step. This result is also confirmed by previous studies (Jeong et al., 2018; C. Kim et al., 2014; Tho et al., 2019; G. Xu et al., 2019).

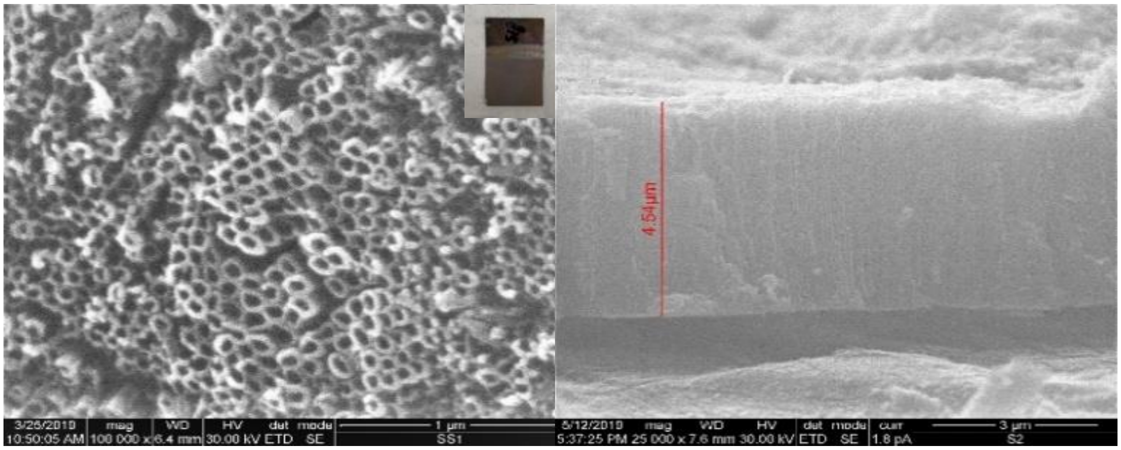

Figure 12: SEM images for the top and cross-sectional view of the TNT

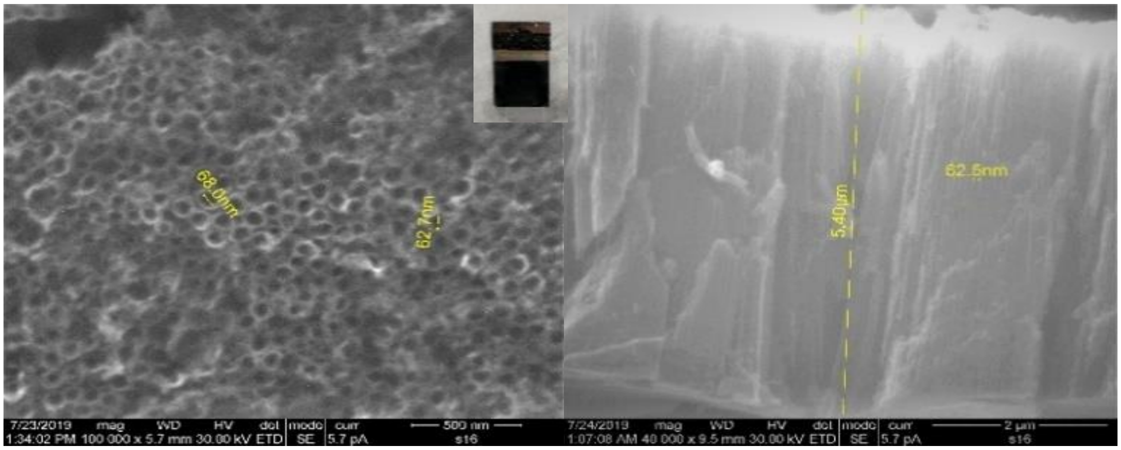

Figure 13: SEM images of the top and cross-sectional view of the BTNT

5.1.1.2. XRD

The crystallinity of BTNT and TNT were compared using XRD, as shown in Figure 14. The comparison of the BTNT and TNT shows that the reduced sample preserved the crystallinity obtained from the annealing step, which is consistent with previous studies (Jeong et al., 2018; C. Kim et al., 2014; H. Li et al., 2014; Wu et al., 2014; G. Xu et al., 2019). The XRD pattern exhibits the primary characteristic peaks of anatase TiO_2 with miller indices (101), (103), (004), (200), (105), and (211) in reference to the JCPDS (PDF 84-1286). The sharpness of the (101) peak at 25.5 degrees indicates the formation of a uniformly crystalline single phase. These results are favorable since anatase is generally preferred for its higher photoactivity attributed to higher bulk transport of electrons and holes to the surface (Luttrell et al., 2014).

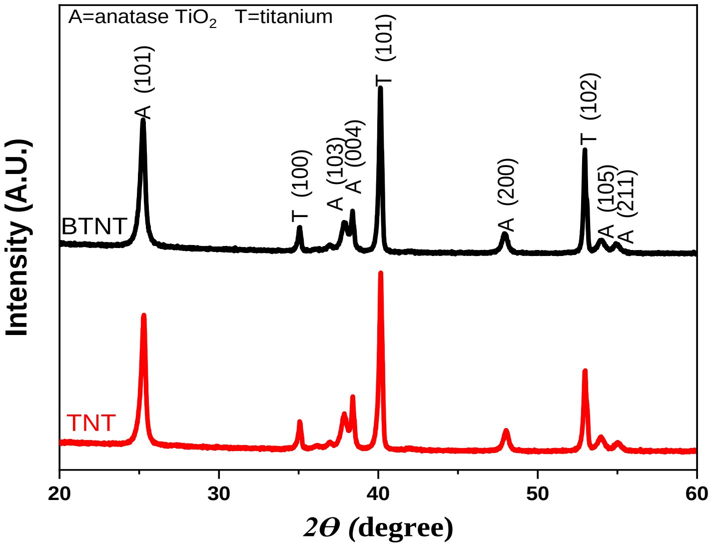

Figure 14: XRD patterns of TNT and BTNT

5.1.1.3. XPS

In order to confirm the reduction of the material, XPS was used to identify chemical composition and oxidation state of the TNT and BTNT. The black coloration achieved by reducing the BTNT is related to the presence of Ti^{3+} and oxygen vacancies due to removing oxygen by electrochemical reduction as shown in equation [2-14] (Ullattil et al., 2018). Figure 15 shows that the Ti *2p* spectra consist of two peaks at 464 eV and 458.6 eV corresponding to Ti $2p_{3/2}$ and Ti $2p_{1/2}$. The negative shift of the BTNT to 463 and 457.5 eV suggests the presence of Ti^{3+} since a reduced element gains electrons and shifts to lower binding energy (G. Xu et al., 2019). This analysis agrees with several literature reports (X. Xu et al., 2020; P. Yan et al., 2015; Zheng et al., 2014; Zhou et al., 2014; Zhu et al., 2018). Table 4 shows the binding energies for the TNT and BTNT as compared to the standard TiO_2 (P25) (Naldoni et al., 2012).

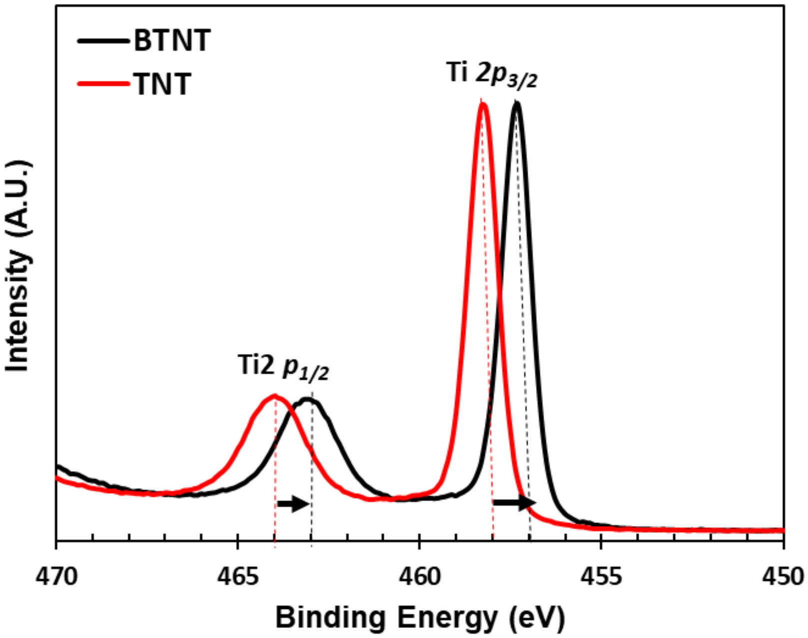

Figure 15:Ti *2p* XPS spectra

Table 4: Binding energies of Ti *2p* and O *1s* as determined by XPS analysis

Sample	Binding Energy (eV) Ti *2p*		Binding Energy (eV) O *1s*
	$2p_{3/2}$	$2p_{1/2}$	
TNT	458.6	464	528
BTNT	457.5	463	530
P25 (Naldoni et al., 2012)	458.46	464.15	529.68

5.1.2. Electrochemical Measurement

5.1.2.1. Cyclic Voltammetry

Figure 16 compares the CVs of BTNT and TNT in a 0.1M KOH aqueous solution. The figure shows that the current density depends on the potential where the positive values witnessed lower current densities indicating higher resistance (Zhu et al., 2018). The triangular shape of the TNT curve is typical for crystalline anatase exhibiting higher electronic resistance as compared to the wider curve for BTNT (Denisov et al., 2020; H. Li et al., 2014; Zhu et al., 2018). The difference in the curve shape of TNT and BTNT and the higher currents observed for the latter indicate that the reduction increased the electronic conductivity. The conductivity enhancement can be explained by the trapping theory where the defects, i.e., Ti^{3+} sites, are energetically localized, and they catch the free electrons from the conduction band (Zhu et al., 2018). The Ti^{3+} states promote a metallic behavior and act as donor centers, thus enhancing charge transport and charge transfer (C. Kim et al., 2014; Wu et al., 2014; X. Yan et al., 2017; Zhou et al., 2014). These trap sites can appear as a cathodic peak around the flat band potential, followed by an increase in cathodic current density due to conductivity improvement (Zhou et al., 2014). The cathodic current increase starts at -0.5 and -0.7V for the BTNT and TNT, respectively, marking the onset for H_2 evolution reaction. In Figure 16, the oxidation potentials for BTNT and TNT were -0.9 V and -1.1V, respectively.

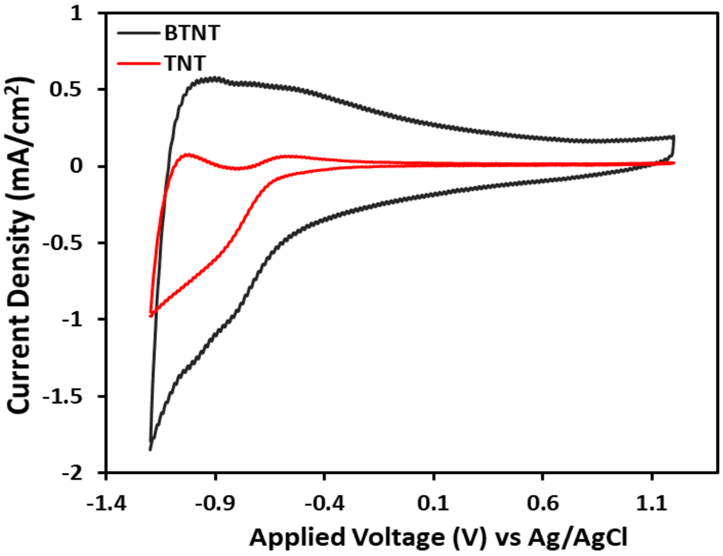

Figure 16: Cyclic voltammograms of TNT and BTNT in 0.1M KOH

5.1.2.2. Linear Sweep Voltammetry

As summarized in Table 5 below, BTNT and TNT can have the same onset potential (Jeong et al., 2018; G. Xu et al., 2019), or the reduced sample may witness a negative shift (Cui et al., 2014; Q. Kang et al., 2013; Z. Li et al., 2020). The onset potential definition is taken as the point where the photocurrent density generated due to the light absorption, has a higher value than dark current density (Jeong et al., 2018). Thus, as demonstrated in Figure 17, the onset is at around -0.5V for both BTNT and TNT, and that is when the photocurrent density (light on) became higher than the dark current (light off). BTNT had a slightly higher photocurrent than TNT up to a voltage of 0.9V; then the difference became more significant where a maximum of 2.5 mA/cm^2 was reached compared to 1.2 mA/cm^2 for the TNT at 1.5V. The sharp increase in current density after

1.1V for both BTNT and TNT showed faster reaction kinetics at the higher voltages. The higher photocurrent indicated increased photoactivity of the BTNT, which is also because of the enhanced conductivity due to the Ti^{3+} states, as explained in the CV section above (Cui et al., 2014; Jeong et al., 2018; Q. Kang et al., 2013; Z. Li et al., 2020; G. Xu et al., 2019).

Table 5: Onset potentials from different studies comparing BTNT and TNT

Reduction method	**Onset potential (V) (TNT/BTNT)**		**Reference**
Simple soaking	0.708	0.581 vs V_{RHE}	(Z. Li et al., 2020)
Electrochemical	1.35	1.35V vs V_{AgAgCl}	(G. Xu et al., 2019)
NaBH$_4$	-1.15	-0.65 vs V_{AgAgCl}	(Tho et al., 2019)
Electrochemical	-0.5	-0.5 vs V_{SCE}	(Jeong et al., 2018)
Aluminium	-0.887	-0.909 vs V_{AgAgCl}	(Cui et al., 2014)
NaBH$_4$	0.16	0.08 vs V_{RHE}	(Q. Kang et al., 2013)
Electrochemical	-0.5	-0.5 vs V_{AgAgCl}	Current study

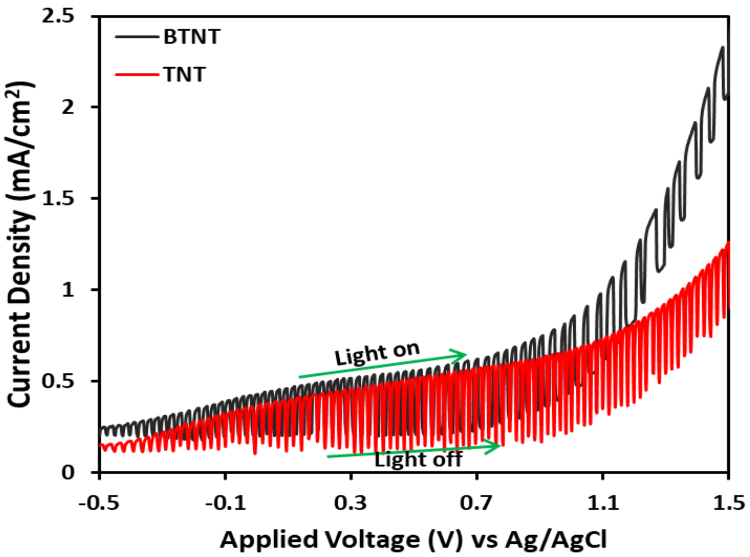

Figure 17:Light-chopped linear sweep voltammogram of TNT and BTNT in 0.1M Na_2SO_3 under simulated sunlight (AM 1.5, 100 mW cm^{-2})

5.1.3. Water Splitting

The current density and the H_2 production rate were measured to assess the fabricated electrodes' performance (BTNT vs. TNT). The comparison is to evaluate the enhancement due to the electrochemical reduction. Table 6 summarizes the reported current densities for BTNT prepared by electrochemical reduction.

Table 6: BTNT current densities as reported in literature

Reduction Method	Current Density (mA\cm^2)	Potential (V)	Electrolyte	pH	Reference
Electrochemical	1.55*	2.4 vs V_{AgAgCl}	Na_2SO_4 (0.05M)	-	(X. Xu et al., 2020)
Electrochemical	0.7	0 vs V_{SCE}	Na_2SO_4 (0.1M)	6.5	(Jeong et al., 2018)
Electrochemical	0.65	0 vs V_{AgAgCl}	KOH (1M)	14	(Chen et al., 2013)
Electrochemical	2.8	1.23 vs. V_{RHE}	KOH (1M)	-	(Z. Zhang et al., 2013)
Electrochemical	0.87 2.26	1 vs V_{AgAgCl}	KOH (1M) H_2SO_4	14 0.7	This study

*(calculated from the given current 5.8mA and area 2.2x1.7cm)

Current density, which is the electric current per unit geometric area of the electrode, is proportional to the reaction rate, i.e., higher current means faster reaction rates (Hernández et al., 2017). In this setup, the current density is measured under three pH conditions, low (acidic), medium (neutral), and high (basic). Low pH accelerates the production of H_2 due to the presence of more H^+ in the solution (G. Zhang et al., 2013). The flat band potential is the required voltage to stretch back the band edges from the bending position to the flat position. This voltage affects the recombination probability. The flat band potential is a function of the pH following the Nernst equation (Maria et al., 2001):

$$E_{fb} = {E_{fb}}^{0} - 0.05915\, pH \quad [5\text{-}1]$$

Where, E_{fb} is the flat band potential and ${E_{fb}}^{0}$ is the standard flat band potential.

Figure 18 compares the current density at the different pH conditions where the neutral and basic conditions gave a lower current than acidic conditions. This is because acidic electrolyte contains a higher amount of H_2 ions (Hong et al., 2009). Furthermore, a negative shift of flat band potential per pH unit enhances the oxidative activity of the holes (Maria et al., 2001). It can also be noticed that the neutral condition had the lowest current, and this can be explained by the point of zero charges of the TiO_2, which happens at around pH = 6.8 (Ojani et al., 2012).

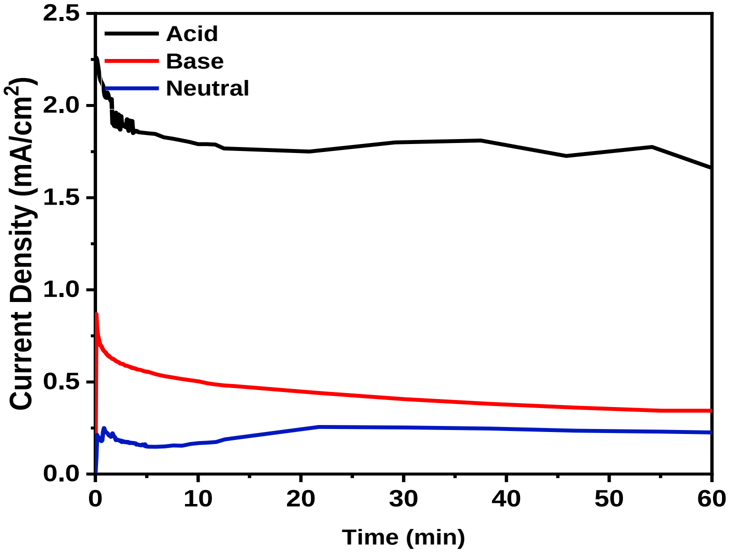

Figure 18: Current density variation at different pH conditions for BTNT at 1V

Figure 19 and Figure 20 show the acidic (pH 0.7~0.9) and basic (pH 13~14) conditions where the BTNT demonstrated superior performance against the TNT. The BTNT demonstrated superior performance against the TNT in both conditions. Higher currents were achieved in acidic conditions reaching a maximum of 2.26 compared to 0.87 mA/cm^2 in basic conditions measured at 1V vs $V_{Ag/AgCl}$.

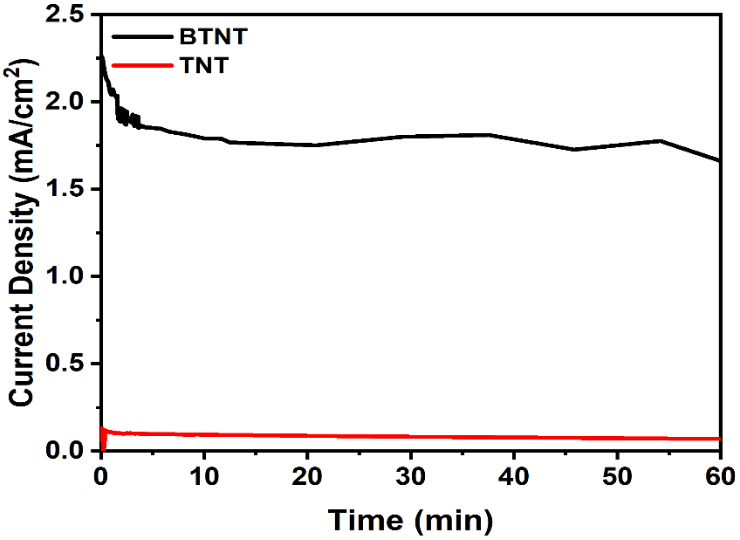

Figure 19:Current density variation in acid at 1V, TNT, and BTNT with an active area of 4cm^2

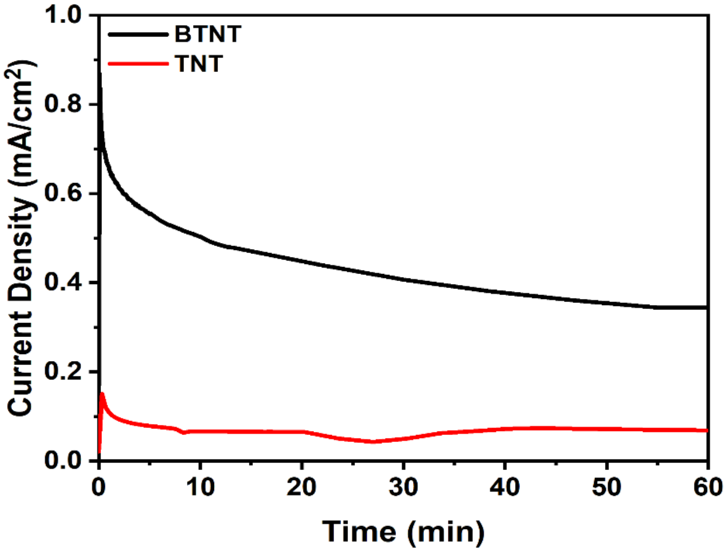

Figure 20: Current density variation in KOH (1M) at 1V, TNT, and BTNT with an active area of 4cm^2

BTNT performance in acidic conditions was furthered tested in a one-hour reaction and at 1V vs. $V_{Ag/AgCl}$ while a residual gas analyzer analyzes the gaseous outlet. Figure 21 shows the H_2 evolution as a percentage over the reaction time for the BTNT and TNT. The TNT resulted in negligible H_2 while the BTNT produced a maximum percentage of 5.15% based on the gas sample volume to the RGA and at an average current density 1.75 mA/cm^2. The decrease in H_2 percentage after 40 minutes is due to the decrease in current density. This in turn suggests that BTNT’s activity degrades which may be due to sulfur poisoning from the acid solution (H. Wang et al., 2019).

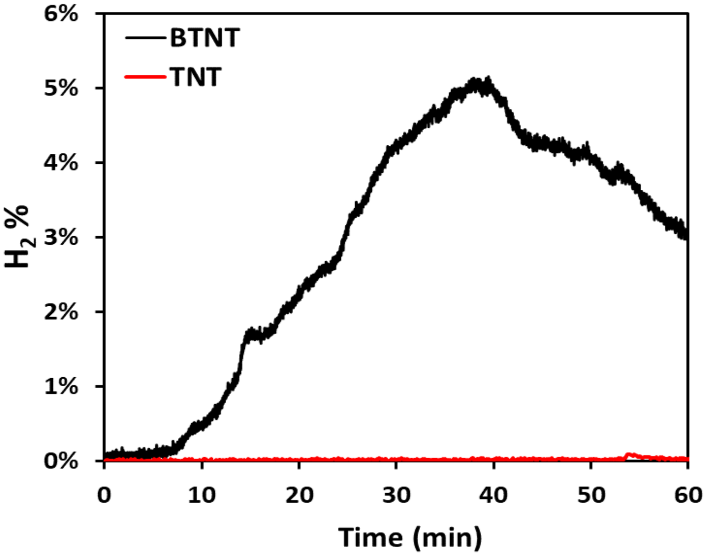

Figure 21: Curves of H_2 evolution as recorded by the RGA for BTNT and TNT in acidic conditions

5.1.4. CO_2 Conversion

From the previous section, the BTNT capability to drive the H_2 generation was proven to be more efficient than TNT. Now, the BTNT's ability to drive CO_2 reduction on gold is analyzed. However, first, validation experiments with platinum and gold were conducted. These experiments were to validate the developed setup and the required conditions for CO_2 reduction. They also served as a benchmark for comparison with BTNT.

To understand the reduction/oxidation reactions on gold cathode, a CV scan is applied from highly negative (reducing) to positive (oxidizing) voltages. The first CV scan is taken for cleaned electrode without electrochemical pretreatment and is shown by the as-received curve in Figure 22. In this scan, two reduction peaks are observed, peaks C and D on the reverse scan, while the oxidation peak is not visible. The reduction peaks are due to the redeposition of gold ions from reducing the gold oxides/hydroxides formed during the forward scan(Cave et al., 2017). A second CV scan is taken after anodic pretreatment to examine its effect on the gold. In this scan, shown as CV1 in Figure 22, the mentioned reduction peaks (C and D) are more pronounced, and three other peaks emerged. Peaks A and B in the forward scan are gold oxide formation peaks, while E is an additional reduction peak. The appearance of multiple peaks indicates that there is a possibility of either several types of oxides/hydroxides formation or different activity states(Kedzierzawski et al., 1994). The CV after the pretreatment shows an evident increase in the gold reduction peak. The increased reduction peaks' areas indicate more reduced gold oxides or hydroxides which are formed in anodic pretreatment (Hoogvliet et al., 2000; H. Kim et al., 2016). Although the created oxide layer is expected to increase active area, it is poorly stable, as confirmed by the third CV scan (CV2), which shows a decrease in reduction peaks' areas as compared to CV1. Nevertheless, comparing CV2 to the as received scan, it is expected a percentage of formed active area is still present.

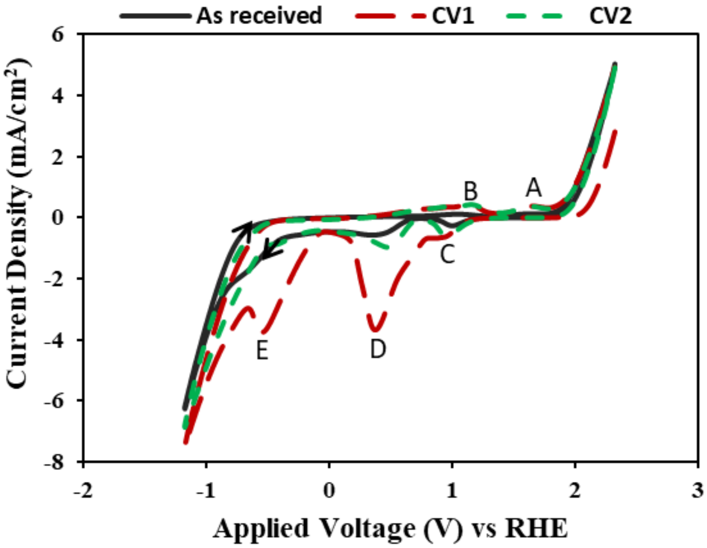

Figure 22: **Cyclic Voltammetry performed in 0.1M $KHCO_3$ at 50 mV/s, the arrows show the direction of the forward and reverse scans. As received scan is before the anodic pretreatment while CV1 and CV2 are after the pretreatment (conducted at 2.3V for 30min). The letters from A to E shows the oxidation and reduction peaks.**

The eletrolyte's pH was measured before and after CO_2 purging, and the readings were 8.52 and 6.81, respectively. These pH values correspond well with the measurements before and after CO_2 saturation in the 0.1M $KHCO_3$ (J. Zhao et al., 2020). Following the cyclic voltammetry, the CO_2 reduction reaction is started by applying the voltage in the range of -0.4 to -1V. An instantaneous color change of the gold to dark brownish is observed, possibly due to partial poisoning from adsorbed species such as potassium, carbon monoxide, or some carbon deposits (Thorson et al., 2012; Wuttig et al., 2016). This deactivation leads to a slight decrease of current over time, as observed in Figure 23. With the increase in voltage from -0.4 to -1V, an increase in current density is observed for both electrodes. For BTNT, the current density increased from 0.36 mA/cm^2 at -0.4V by 2.8 mA/cm^2 and 4.06 mA/cm^2 when voltage is swept from -0.4 to -0.7V and from -0.7 to 1V, respectively. For Pt electrode, the current density increased from 0.36 mA/cm^2 at -0.4V, by 2.5 mA/cm^2 and 3.15 mA/cm^2 from when voltage is swept from -0.4 to -0.7 V and from -0.7 to 1V, respectively. It is worth noting that at -1V, the two electrodes' current densities are comparable. However, with the increase in the voltage, Pt electrode results in a significant increase in H_2 production as compared to BTNT as shown in Figure 24. This is due to a higher activity of the Pt electrode, where an increase in current density enhanced the reaction rate. On the other hand, BTNT showed less H_2 production than Pt electrode, which indicates that the electrode has a limited activity to drive the reduction reaction. From Figure 24, the maximum H_2 concentration was 35 and 10 ppm at -1V for Pt and BTNT, respectively.

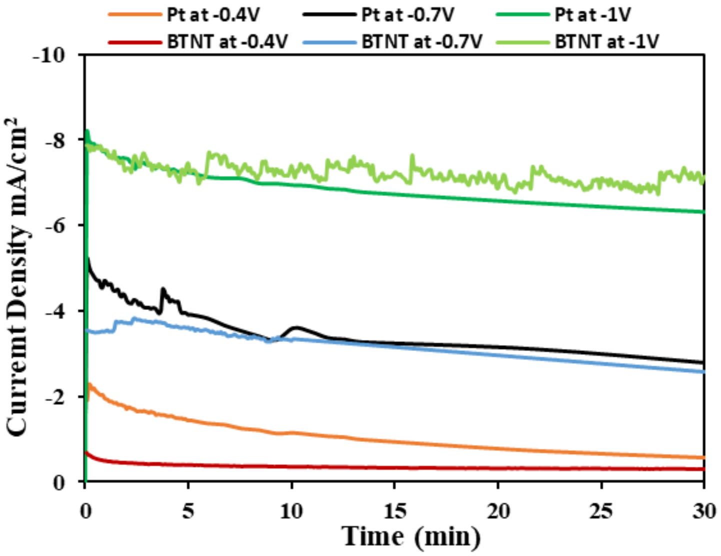

Figure 23: Comparison Current density versus time of representative experiments with Pt and BTNT.

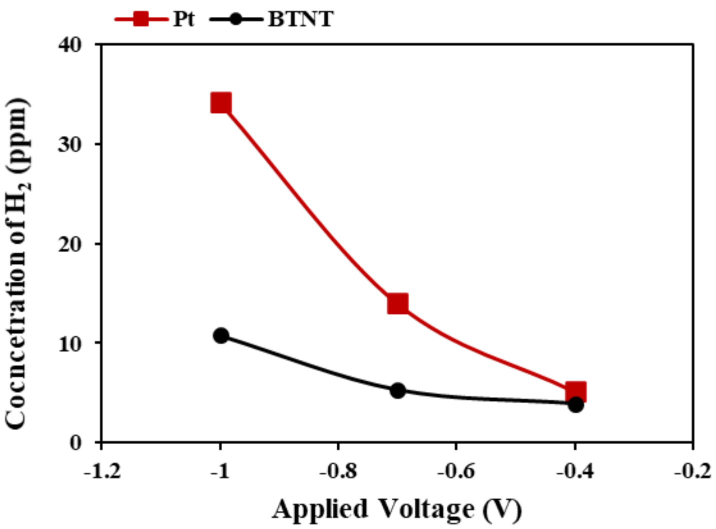

Figure 24: H_2 concentration at different voltages as detected by the RGA (Pt vs. BTNT)

The analysis of CO_2 reduction reaction products using FTIR revealed the presence of free CO stretching frequency at ~2100-2200 cm^{-1}, which confirms the activity of the two electrodes (Acree et al.). As shown in Figure 25, at a low potential of -0.4V, the two electrodes did not produce any CO, which indicates that the onset potential for CO_2 reduction to CO is not reached. On varying the voltage from -0.4 to -0.7V, CO stretching is observed for Pt electrode, while for BTNT, it is observed at -1V. Moreover, CO stretching intensity increases with the applied voltage which is clearly observed for the Pt. In all cases, BTNT showed lower intensities compared to Pt, indicating lower rate of CO production. This essentially means that BTNT electrode requires a higher overpotential for driving the CO_2 reduction reaction.

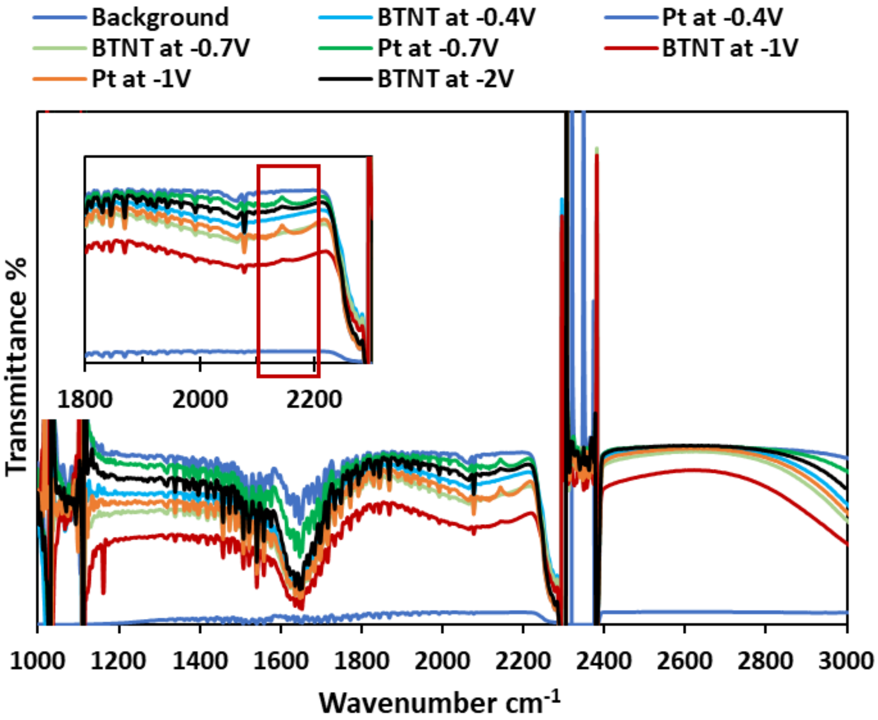

Figure 25: CO detection by FTIR while the inset shows the zoomed-in area of interest

5.1.5. Influence of Electrolyte Concentration and Stirring Rate

The electrochemical CO_2 to syngas is influenced by the applied voltage/current density, mass transfer limitations, electrolyte concentration, and electrocatalyst (Gattrell et al., 2006). The applied voltage effect is visible in the above discussion, where higher voltages led to higher H_2 and CO (Figure 24 and Figure 25). Increasing the current density can be through the applied voltage or electrolyte concentration. More concentrated electrolytes have more ions for charge transport. Two electrolyte concentrations were studied (0.1M and 0.5M) $KHCO_3$, where the current density at higher concentration is almost twice the lower concentration, as depicted in Figure 26. This increase in current is reflected in the H_2 rate increase of around 66% more in the concentrated electrolyte.

However, on a visual inspection of gold cathode, the darker shade in the 0.5M electrolyte is related to the deactivation of electrocatalyst, which also explains the faster decrease in current density by 6.1mA/cm^2 at 0.5M compared to a decrease of 2.4 mA/cm^2 at 0.1M. The cathode deactivation can occur due to metals deposition from electrolyte impurities or surface-bound intermediates (Ahangari et al., 2020). To mitigate this phenomenon, 0.1M electrolyte solution was used for all the electrochemistry experiments. Promoting mass transfer is one way to enhance the adsorption/desorption of reactants/products from active sites (Goyal et al., 2020). This explains the observed increase in H_2 upon higher stirring, as shown in Figure 27.

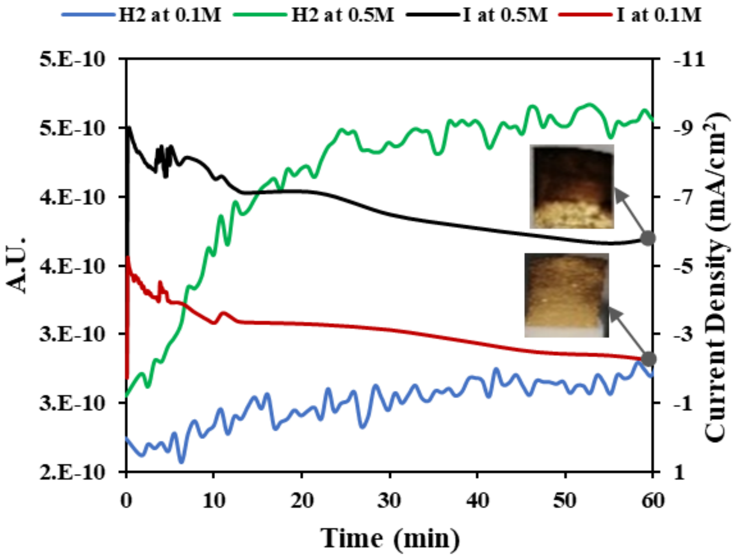

Figure 26: Effect of concentration on H_2 and current density (I) with the change of gold cathode color after the reaction

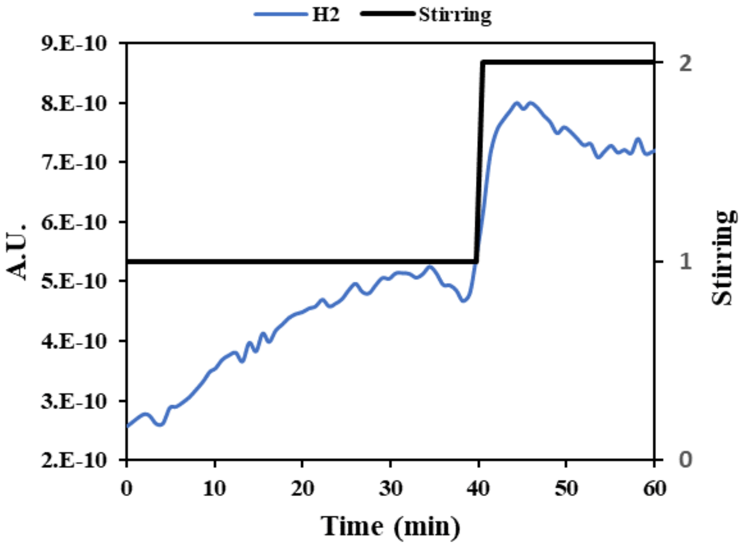

Figure 27: Effect of stirring on H_2

5.2. Environmental and Economic Analysis

After the proof of concept for using BTNT in electrochemical CO_2 conversion to syngas, the economic impact of replacing BTNT with Pt is investigated. From the experimental analysis and based on the H_2 concentration from using both electrodes, the Pt is at least 3.18 times more active than BTNT. This is a rough estimate as it does not include the durability of the material. Nonetheless, based on the metal cost per weight, the Pt (43 $/g) is 390 times more expensive than titanium (0.11 $/g) (Industries, 2021; Johnson, 2021). It is expected that the cost gap is less than 390 times when the cost of the BTNT synthesis is added, however, the BTNT will still be cheaper since the synthesis method developed in this study has the advantage of being low cost and non-energy intensive. Therefore, the BTNT is a promising material to reduce the overall cost of the electrochemical system.

Moreover, the developed experimental setup is assessed in terms of sustainability and compared to commercialized electrochemical systems from Siemens and Dioxide Materials companies. As shown in Figure 10, there are two scenarios: scenario (a) uses one electrolyzer to convert CO_2 and H_2O streams to syngas at the specified ratio; and scenario (b) uses two electrolyzers: one to convert CO_2 to CO and the other to produce H_2 from H_2O. Scenario (a) is studied by two cases: the experimental setup and Siemens reported syngas electrolyzer and scenario (b) is studied through a commercial CO electrolyzer developed by Dioxide Materials company coupled with a commercial H_2 electrolyzer. To conclude the analysis, a preliminary sensitivity study is implemented to highlight the most crucial parameter and set the targets for the future commercialization. The sustainability assessment and the comparative analysis are based on the total CO_2 emissions and the operating cost.

Table 7 shows the comparison of literature-reported electrochemical systems with the experimental setup. The experimental setup has the highest emissions and operating cost because of the low conversion. The lower conversion increases the CO_2 stream demand. The experimental setup is inherently limited by the slow diffusion of CO_2 to the electrocatalyst and the CO_2 solubility. This limitation can be overcome by direct contact of the gas-phase with the cathode through the use of gas diffusion electrodes (GDEs) (Higgins et al., 2019). Siemens and Dioxide Materials systems use more efficient electrochemical cells based on GDEs that can achieve higher currents and conversions. Therefore, their CO_2 emissions and the operating cost are lower than the experimental setup. Dioxide Materials system resulted in negative CO_2 emissions which means the system is converting more CO_2 than the emitted. The lower CO_2 emissions and costs of this system is because of its higher energy efficiency translating to lower electricity demand.

Table 7: Total emissions and cost comparison

Electrochemical Cases	**Scenario**	**Total emissions (kg_{CO2}/kg_{syngas})**	**OPEX ($\$/kg_{syngas}$)**
Experimental setup	Direct step	56.59	28.52
Siemens	Direct step	0.78	2.89
Dioxide Materials	Dual step	-0.21	1.36

To compare with conventional benchmark the work of Afzal et al. was used from which the dry methane reforming (DRM) has total emissions of 0.03 kg_{CO2}/kg_{syngas} and OPEX of 0.065 $\$/kg_{syngas}$ (Afzal et al., 2018). The only system that has less emissions than DRM is the Dioxide Materials system. Afzal et al. calculated the OPEX for DRM, assuming that the CO_2 stream is available at zero cost (Afzal et al., 2018). The CO_2 stream for electrochemical CO_2 reduction requires treatment since a high purity is required, therefore it is considered at a cost of 30$/ton (De Luna et al., 2019). As shown in Table 7, all the analyzed electrochemical systems resulted in higher OPEX compared to 0.065 $\$/kg_{syngas}$ of the DRM. The main factors contributing to this higher OPEX are renewable electricity price and energy efficiency confirming previous techno-economic assessments (Adnan et al., 2020; De Luna et al., 2019).

A sensitivity study was conducted to understand the impact of different parameters (i.e., current density, energy efficiency, faradaic efficiency, and reduction of CO_2 to CO) on CO_2 emissions and the electrochemical systems' total cost. The base case is assumed as a direct syngas system, and its specifications are as shown in Table 8.

Table 8: Base case used for the sensitivity analysis

Parameter	**Base**
Current density (mA/cm^2)	120.0
Applied voltage (V)	2.5
Overpotential (V)	1.2
Faradaic efficiency	50%
Energy efficiency	53%
Conversion	20%
Price of CO_2 ($/kg)	0.03
Electrolyzer Cost ($/m^2)	1840
Price of electricity ($/kWh)	0.07

To compare the effects of different parameters, only one parameter was varied at a time while the rest was at the base case value. The change was fixed at either a high value which is 50% more than the base value, or low, i.e., 50% less than the base value. Figure 28 and Figure 29 show that energy efficiency is the most critical parameter for total emissions and total cost. Energy efficiency is related to overpotential (extra voltage above equilibrium potential to drive reaction), which is the bottleneck of improving the process. Faradaic efficiency highlights the difference between direct and dual-step systems. For high faradaic efficiency, a second electrolyzer is required to supply H_2. For low faradaic efficiency, extra H_2 is produced, which can generate revenue, but increases the separation cost to alter the syngas ratio. Assuming the revenue from H_2 normalizes separation cost, dual-step minimized emissions and cost compared to a direct-step process. At lower faradaic efficiency, H_2 is produced inefficiently from syngas electrolyzer, which has lower energy efficiency than commercial H_2 electrolyzer. The conversion of CO_2 to CO had a significant impact on emissions because of the CO_2 stream emissions, while current density did not have an impact on emissions as it only affects electrolyzer area. Finally, the effect of conversion and current density appears to be equivalent on total cost.

In comparing the impact of varying CO_2 prices, electricity, and electrolyzer, an increase or decrease in CO_2 price or electrolyzer cost by 50% affects total cost by 6%, while electricity price affects total cost by 37%. Pushing energy efficiency to 70% and lowering electricity price to 4 cents/kWh is still insufficient for the base case to have lower OPEX than DRM. Hence, an incentive is required for the electrochemical system to break even with DRM. This can be through carbon credits, where the minimum is calculated to be 0.28 \$/kgCO_2 to achieve an OPEX of 0.06 \$/kg syngas for net CO_2 fixation of 0.86 kgCO_2/kg syngas.

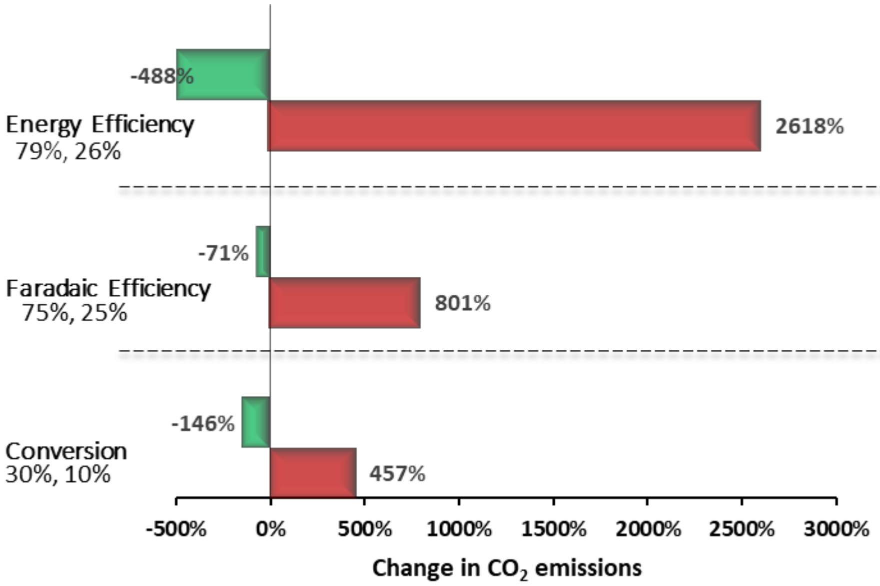

Figure 28: Effect of varying energy efficiency, faradaic efficiency, and conversion on the total CO_2 emissions.

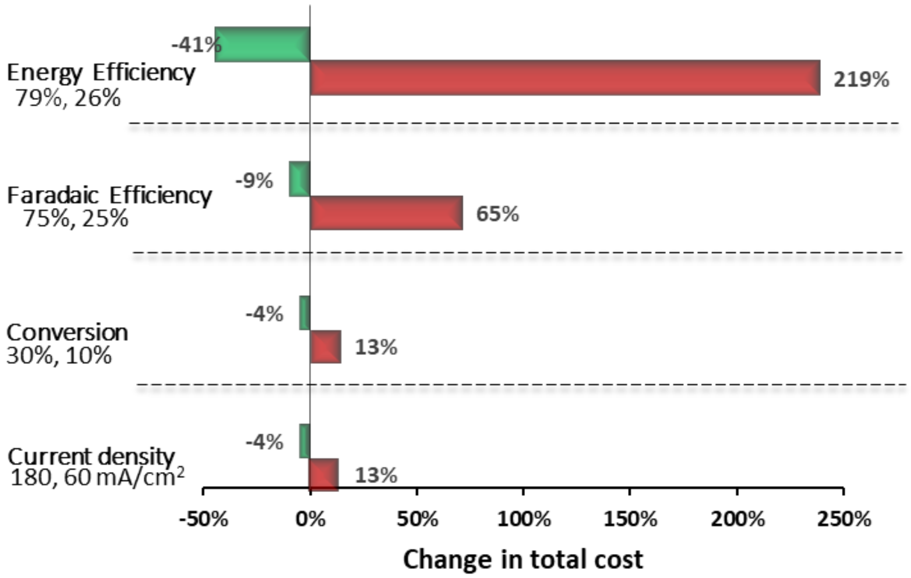

Figure 29: Effect of varying energy efficiency, faradaic efficiency, and conversion on the total cost.

Starting from the base case as in Table 8, and to use the developed experimental system which has a conversion of 0.15%, 128 cells connected in series are needed to reach a conversion of 20% and each cell will have an area of 1.04 m^2. The outlet stream will need to go through a separation process to separate the syngas from the CO_2 which is then recycled back to the cells. The net fixation of CO_2 from this process will be -0.47 kg CO_2/ kg syngas. Currently, Siemens is developing a pilot scale for production of syngas from CO_2 consisting of 10 cells where the area of the cell is 300 cm^2 giving a total area of 3000 cm^2 (Hubertus, 2020).

6. CONCLUSIONS

The main contribution of this study that it proves the capability of the BTNT to drive the CO_2 reduction to syngas through a developed electrochemical setup. This has been achieved after following the described methods. In summary, BTNT was successfully obtained with highly ordered nanotube structures using an anodization-electrochemical reduction approach. This specific synthesis approach is chosen based on its potential scalability due to its simplicity yet effectiveness to obtain the desired characteristics. Also, this approach can easily be integrated in a sustainable scheme based on renewable energy as it uses electricity as the main energy source. The confirmation of the desired morphology and crystallinity was done using SEM and XRD characterization techniques which compared the TNT and BTNT and showed the similar nanotubular morphology and crystalline structure. These results also confirmed that both the morphology and crystalline structure were preserved after the reduction reaction. The change on the BTNT due to the reduction reaction is highlighted by the XPS results which shows a shift in the Ti*2p* peaks to lower binding energies. This shift indicates that Ti^{4+} moved to a lower oxidation state (Ti^{3+}) by gaining electrons during the electrochemical reduction step. Through the electrochemical tests, BTNT showed higher conductivity and photocurrent density compared to the white TNT. This superior performance is attributed to the Ti^{3+} presence. The synthesized material has also shown more activity in producing H_2 as compared with TNT. The highest performance is achieved in acidic conditions where the maximum percentage based on the gas sample volume reached 5.15% at an average current density of 1.75 mA/cm^2. Then, the BTNT was investigated as an anode in an electrochemical cell with a gold cathode to produce a mixture of CO/H_2. A qualitative model based on FTIR and RGA was used to prove and compare the capability of the BTNT to produce CO/H_2 with Pt. The results indicated that the minimum voltage for the BTNT to drive the CO_2 reduction to CO is -1V while the Pt requires -0.7V. Moreover, the H_2 concentration as detected by the RGA and the intensity of CO stretching from the FTIR, were lower for the BTNT as compared with the Pt at the same voltage. This concluded that the overpotential for the BTNT is higher than the Pt and further enhancement on the activity is required to obtain comparable performance.

From the experimental analysis and based on the H_2 concentration as detected by RGA, the Pt is at least 3.18 times more active than BTNT however, Pt is almost 390 times more expensive than BTNT. The huge difference in price encourages the development of an electrochemical system based on BTNT despite the lower activity. The sustainability of the experimental setup to produce CO/H_2 using BTNT, was assessed based on CO_2 emissions and cost. The comparison showed that due to the low CO_2 conversion, the setup had higher emissions and OPEX. The electrochemical systems have higher operating cost compared to DRM, which is mainly due to their large energy demand considering the cost of renewable electricity.

Through the sensitivity study, it is found that the critical parameter is the overpotential which needs to be substantially lowered to decrease both costs and emissions. For the electrochemical systems to have lower OPEX than DRM, an incentive is necessary. Therefore, to make electrochemical CO_2 to syngas economically attractive, policies that support the deployment of renewable energy and the utilization of CO_2 are vital. Nevertheless, scaling up this system can offer a mobile solution which is a viable way to store the intermittent renewable energy into chemical bonds. With the status of the developed experimental setup and to boost the conversion a scaled-up system can be comprised of 128 cells where each cell has an area of 1.04 m^2 followed by a separation process. The unconverted CO_2 after the separation process is recycled to the cells. The net fixation of CO_2 from such a scaled-up system will be -0.47 kg CO_2/ kg syngas for a production of 1071.43 kg syngas/day. Finally, as will be detailed in the recommendations, there is room for improvement especially on enhancing the activity of the BTNT and the overall efficiency of the system.

7. RECOMMENDATIONS FOR FUTURE STUDIES

Following the conclusion of this work, several opportunities for future studies are recommended to achieve the ultimate goal of commercializing BTNT based systems for CO_2 conversion and water splitting. The first recommended step is the modification of the BTNT to enhance its activity and this can be done by several methods such as localized surface plasmon of metals into the BTNT (Paul et al., 2018) or incorporation of conductive materials and electron acceptors such as carbon nanotubes (Naffati et al., 2020) or graphene (Padmanabhan et al., 2021). These modifications are expected to further facilitate charge mobility, reduce the electron/hole recombination, and narrow the bandgap. Moreover, detailed investigation to establish the relationship between the performance and the BTNT characteristics is encouraged through other characterization techniques such as Transmission electron microscopy (TEM) and Brunauer-Emmett-Teller (BET) surface area analysis. Also, it is recommended to study and estimate the electrochemically active surface area (ECSA) to provide accurate comparison with literature reported and benchmark materials.

Following the modification of the BTNT, testing its performance in photoelectrochemical cell based on gas diffusion electrodes is important to improve the current density of the system and utilize the photocatalytic ability of the BTNT. Furthermore, this system should be connected to a sensitive gas chromatography to allow precise measurement of the produced syngas. In addition, to the gaseous analysis, liquid analysis through Nuclear magnetic resonance spectroscopy (NMR) is important for the calculation of the faradaic efficiency.

In the current study, the used cathode was gold however, for the future scalability, cheaper alternatives that have comparable selectivity towards CO are needed, and this is an active research area (Cheng et al., 2018). Finally, a detailed sustainability analysis where the pretreatment of the CO_2 source and the downstream processes involving the produced syngas to yield a the desired end product such as methanol should be considered.

It is worth mentioning that BTNT has also a potential in many other applications where TiO_2 is being investigated including water treatment, dye-sensitized solar cells, batteries, and supercapacitors. For further details the reader is encouraged to refer to the cited review paper (Ullattil et al., 2018).

REFERENCES

1. Acree, W., & Chickos, J. Infrared Spectra. In P. Linstrom & W. Mallard (Eds.), *NIST Chemistry WebBook, NIST Reference Standard Database Number 69*.
2. Adán, C., Marugán, J., Sánchez, E., Pablos, C., & van Grieken, R. (2016). Understanding the effect of morphology on the photocatalytic activity of TiO2 nanotube array electrodes. *Electrochimica Acta, 191*, 521-529. doi:10.1016/j.electacta.2016.01.088
3. Adnan, M. A., & Kibria, M. G. (2020). Comparative techno-economic and life-cycle assessment of power-to-methanol synthesis pathways. *Applied Energy, 278*. doi:10.1016/j.apenergy.2020.115614
4. Afzal, S., Sengupta, D., Sarkar, A., El-Halwagi, M., and, & Elbashir, N. (2018). Optimization Approach to the Reduction of CO2 Emissions for Syngas Production Involving Dry Reforming. *ACS Sustainable Chemistry & Engineering, 6*(6), 7532-7544. doi:10.1021/acssuschemeng.8b00235
5. Ahangari, H. T., & Marshall, A. T. (2020). Preventing the Deactivation of Gold Cathodes During Electrocatalytic CO2 Reduction While Avoiding Gold Dissolution. *Electrocatalysis, 11*(1), 25-34. doi:10.1007/s12678-019-00564-z
6. Ahmed, M., & Dincer, I. (2019). A review on photoelectrochemical hydrogen production systems: Challenges and future directions. *International Journal of Hydrogen Energy, 44*(5), 2474-2507. doi:10.1016/j.ijhydene.2018.12.037
7. Akhtar, K., Khan, S. A., Khan, S. B., & Asiri, A. M. (2018). Scanning Electron Microscopy: Principle and Applications in Nanomaterials Characterization. In *Handbook of Materials Characterization* (pp. 113-145).
8. Al Baroudi, H., Awoyomi, A., Patchigolla, K., Jonnalagadda, K., & Anthony, E. J. (2021). A review of large-scale CO2 shipping and marine emissions management for carbon capture, utilisation and storage. *Applied Energy, 287*. doi:10.1016/j.apenergy.2021.116510
9. Amano, F., Nakata, M., Yamamoto, A., & Tanaka, T. (2016). Effect of Ti3+ Ions and Conduction Band Electrons on Photocatalytic and Photoelectrochemical Activity of Rutile Titania for Water Oxidation. *The Journal of Physical Chemistry C, 120*(12), 6467-6474. doi:10.1021/acs.jpcc.6b01481
10. Andrade, J. D. (1985). X-ray Photoelectron Spectroscopy (XPS). In *Surface and Interfacial Aspects of Biomedical Polymers*. Boston, MA: Springer.
11. Brian, M. T. (2013). Electroanalytical Chemistry. *Basics of Analytical Chemistry and Chemical Equilibria*, 293-339. doi:https://doi.org/10.1002/9781118647042.ch8
12. Bruckner, T., Fulton, L., Hertwich, E., McKinnon, A., Perczyk, D., Roy, J., . . . Wiser, R. U. (2014). *Annex III: Technology-specific cost and performance parameters. In: Climate Change 2014: Mitigation of Climate Change.* Retrieved from Cambridge, United Kingdom and New York, NY, USA.:
13. Bunaciu, A. A., Udristioiu, E. G., & Aboul-Enein, H. Y. (2015). X-ray diffraction: instrumentation and applications. *Crit Rev Anal Chem, 45*(4), 289-299. doi:10.1080/10408347.2014.949616

14. Carmo, M., Fritz, D. L., Mergel, J., & Stolten, D. (2013). A comprehensive review on PEM water electrolysis. *International Journal of Hydrogen Energy, 38*(12), 4901-4934. doi:10.1016/j.ijhydene.2013.01.151
15. Carmo, M., & Stolten, D. (2019). Chapter 4 - Energy Storage Using Hydrogen Produced From Excess Renewable Electricity: Power to Hydrogen. In P. E. V. de Miranda (Ed.), *Science and Engineering of Hydrogen-Based Energy Technologies* (pp. 165-199): Academic Press.
16. Cave, E. R., Montoya, J. H., Kuhl, K. P., Abram, D. N., Hatsukade, T., Shi, C., . . . Jaramillo, T. F. (2017). Electrochemical CO2 reduction on Au surfaces: mechanistic aspects regarding the formation of major and minor products. *Phys Chem Chem Phys, 19*(24), 15856-15863. doi:10.1039/c7cp02855e
17. Chang, X., Wang, T., Zhang, P., Wei, Y., Zhao, J., & Gong, J. (2016). Stable Aqueous Photoelectrochemical CO2 Reduction by a Cu2 O Dark Cathode with Improved Selectivity for Carbonaceous Products. *Angew Chem Int Ed Engl, 55*(31), 8840-8845. doi:10.1002/anie.201602973
18. Chen, X., Ye, S., Linfeng, L., Chuanwei, C., Dongfang, L., Xiaohong, F., . . . Dongdong, L. (2013). Electrochemically hydrogenated TiO2 nanotubes with improved photoelectrochemical water splitting performance. *Nanoscale Research Letters*.
19. Cheng, Y., Zhao, S., Johannessen, B., Veder, J. P., Saunders, M., Rowles, M. R., . . . Jiang, S. P. (2018). Atomically Dispersed Transition Metals on Carbon Nanotubes with Ultrahigh Loading for Selective Electrochemical Carbon Dioxide Reduction. *Adv Mater, 30*(13), e1706287. doi:10.1002/adma.201706287
20. Cho, S., Jang, J.-W., Lee, K.-H., & Lee, J. S. (2014). Research Update: Strategies for efficient photoelectrochemical water splitting using metal oxide photoanodes. *APL Materials, 2*(1). doi:10.1063/1.4861798
21. Ciobanu, M., Wilburn, J. P., Krim, M. L., & Cliffel, D. E. (2007). Chapter one: Fundamentals. In C. G. Zoski (Ed.), *Handbook of Electrochemistry* (pp. 3-29). Amsterdam: Elsevier.
22. Cui, H., Zhao, W., Yang, C., Yin, H., Lin, T., Shan, Y., . . . Huang, F. (2014). Black TiO2 nanotube arrays for high-efficiency photoelectrochemical water-splitting. *J. Mater. Chem. A, 2*(23), 8612-8616. doi:10.1039/c4ta00176a
23. Daéid, N. N. (2005). FORENSIC SCIENCES | Systematic Drug Identification. In P. Worsfold, A. Townshend, & C. Poole (Eds.), *Encyclopedia of Analytical Science (Second Edition)* (pp. 471-480). Oxford: Elsevier.
24. David, J., & Herzog, H. (2001). *The cost of carbon capture*: CSIRO Publishing, Collingwood, Vic. (Australia);.
25. de Brito, J. F., Tavella, F., Genovese, C., Ampelli, C., Zanoni, M. V. B., Centi, G., & Perathoner, S. (2018). Role of CuO in the modification of the photocatalytic water splitting behavior of TiO2 nanotube thin films. *Applied Catalysis B: Environmental, 224*, 136-145. doi:10.1016/j.apcatb.2017.09.071
26. De Luna, P., Hahn, C., Higgins, D., Jaffer, S. A., Jaramillo, T. F., & Sargent, E. H. (2019). What would it take for renewably powered electrosynthesis to

displace petrochemical processes? *Science, 364*(6438). doi:10.1126/science.aav3506

27. Denisov, N., Qin, S., Cha, G., Yoo, J., & Schmuki, P. (2020). Photoelectrochemical properties of "increasingly dark" TiO2 nanotube arrays. *Journal of Electroanalytical Chemistry*. doi:10.1016/j.jelechem.2020.114098
28. Dikova, T. D., Hahm, M. G., Hashim, D. P., Narayanan, N. T., Vajtai, R., & Ajayan, P. M. (2014). Mechanism of TiO2 Nanotubes Formation on the Surface of Pure Ti and Ti-6Al-4V Alloy. *Advanced Materials Research, 939*, 655-662. doi:10.4028/www.scientific.net/AMR.939.655
29. DOE. (2015). Technical Targets for Hydrogen Production from Electrolysis
30. Elgrishi, N., Rountree, K. J., McCarthy, B. D., Rountree, E. S., Eisenhart, T. T., & Dempsey, J. L. (2017). A Practical Beginner's Guide to Cyclic Voltammetry. *Journal of Chemical Education, 95*(2), 197-206. doi:10.1021/acs.jchemed.7b00361
31. Fujishima, A., & Honda, K. (1972). Electrochemical Photolysis of Water at a Semiconductor Electrode. *Nature, 238*(5358), 37-38. doi:10.1038/238037a0
32. Ganesh, I., Kumar, P. P., Annapoorna, I., Sumliner, J. M., Ramakrishna, M., Hebalkar, N. Y., . . . Sundararajan, G. (2014). Preparation and characterization of Cu-doped TiO2 materials for electrochemical, photoelectrochemical, and photocatalytic applications. *Applied Surface Science, 293*, 229-247. doi:10.1016/j.apsusc.2013.12.140
33. Gao, J., Shen, Q., Guan, R., Xue, J., Liu, X., Jia, H., . . . Wu, Y. (2020). Oxygen vacancy self-doped black TiO2 nanotube arrays by aluminothermic reduction for photocatalytic CO2 reduction under visible light illumination. *Journal of CO2 Utilization, 35*, 205-215. doi:10.1016/j.jcou.2019.09.016
34. Gattrell, M., Gupta, N., & Co, A. (2006). A review of the aqueous electrochemical reduction of CO2 to hydrocarbons at copper. *Journal of Electroanalytical Chemistry, 594*(1), 1-19. doi:10.1016/j.jelechem.2006.05.013
35. Goyal, A., Marcandalli, G., Mints, V. A., & Koper, M. T. M. (2020). Competition between CO2 Reduction and Hydrogen Evolution on a Gold Electrode under Well-Defined Mass Transport Conditions. *J Am Chem Soc, 142*(9), 4154-4161. doi:10.1021/jacs.9b10061
36. Grim, R. G., Huang, Z., Guarnieri, M. T., Ferrell, J. R., Tao, L., & Schaidle, J. A. (2020). Transforming the carbon economy: challenges and opportunities in the convergence of low-cost electricity and reductive CO2 utilization. *Energy & Environmental Science, 13*(2), 472-494. doi:10.1039/c9ee02410g
37. Haas, T., Krause, R., Weber, R., Demler, M., & Schmid, G. (2018). Technical photosynthesis involving CO2 electrolysis and fermentation. *Nature Catalysis, 1*(1), 32-39. doi:10.1038/s41929-017-0005-1
38. Hernández, S., Amin Farkhondehfal, M., Sastre, F., Makkee, M., Saracco, G., & Russo, N. (2017). Syngas production from electrochemical reduction of CO2: current status and prospective implementation. *Green Chemistry, 19*(10), 2326-2346. doi:10.1039/c7gc00398f

39. Higgins, D., Hahn, C., Xiang, C., Jaramillo, T. F., & Weber, A. Z. (2019). Gas-Diffusion Electrodes for Carbon Dioxide Reduction: A New Paradigm. *ACS Energy Letters, 4*(1), 317-324. doi:10.1021/acsenergylett.8b02035
40. Hong, W. S., Park, J. H., & Han, G. Y. (2009). Optimization of conditions for hydrogen production from anodized TiO2 nanotube-based photoelectrochemical cells. *J Nanosci Nanotechnol, 9*(12), 7293-7297. doi:10.1166/jnn.2009.1770
41. Hoogvliet, J. C., Dijksma, M., Kamp, B., & van Bennekom, W. P. (2000). Electrochemical Pretreatment of Polycrystalline Gold Electrodes To Produce a Reproducible Surface Roughness for Self-Assembly: A Study in Phosphate Buffer pH 7.4. *Analytical Chemistry, 72*(9), 2016-2021. doi:10.1021/ac991215y
42. Hori, Y. (2008). Electrochemical CO2 Reduction on Metal Electrodes. In C. G. Vayenas, R. E. White, & M. E. Gamboa-Aldeco (Eds.), *Modern Aspects of Electrochemistry* (pp. 89-189). New York, NY: Springer New York.
43. Hoyer, P. (1996). Formation of a Titanium Dioxide Nanotube Array. *Langmuir, 12*(6), 1411-1413. doi:10.1021/la9507803
44. Hubertus, B. (2020). A climate killer is turned into feedstock: Using CO_2 and hydrogen for sustainable chemicals
45. IEA. (2021a). *Global Energy Review 2021*. Retrieved from Paris: https://www.iea.org/reports/global-energy-review-2021
46. IEA. (2021b). *Net Zero by 2050*. Retrieved from Paris: https://www.iea.org/data-and-statistics/data-product/net-zero-by-2050-scenario
47. IEA. (2021c). *Sustainable Development Scenario*. Retrieved from Paris: https://www.iea.org/reports/world-energy-model/sustainable-development-scenario#a-cleaner-and-more-inclusive-energy-future
48. Industries, N. S. (2021). Titanium Manufacturers.
49. Iqbal, M. Z., & Siddique, S. (2018). Recent progress in efficiency of hydrogen evolution process based photoelectrochemical cell. *International Journal of Hydrogen Energy, 43*(46), 21502-21523. doi:10.1016/j.ijhydene.2018.09.157
50. Ismail, A. A., & Bahnemann, D. W. (2014). Photochemical splitting of water for hydrogen production by photocatalysis: A review. *Solar Energy Materials and Solar Cells, 128*, 85-101. doi:10.1016/j.solmat.2014.04.037
51. Jarvis, S. M., & Samsatli, S. (2018). Technologies and infrastructures underpinning future CO 2 value chains: A comprehensive review and comparative analysis. *Renewable and Sustainable Energy Reviews, 85*, 46-68. doi:10.1016/j.rser.2018.01.007
52. Jeong, H. W., Park, K. J., Han, D. S., & Park, H. (2018). High efficiency solar chemical conversion using electrochemically disordered titania nanotube arrays transplanted onto transparent conductive oxide electrodes. *Applied Catalysis B: Environmental, 226*, 194-201. doi:10.1016/j.apcatb.2017.12.043
53. Johnson, M. (2021). Johnson Matthey Base Prices in US$ per troy oz.
54. Jouny, M., Luc, W., & Jiao, F. (2018). General Techno-Economic Analysis of CO2 Electrolysis Systems. *Industrial & Engineering Chemistry Research, 57*(6), 2165-2177. doi:10.1021/acs.iecr.7b03514

55. Joy, J., Mathew, J., & George, S. C. (2018). Nanomaterials for photoelectrochemical water splitting – review. *International Journal of Hydrogen Energy, 43*(10), 4804-4817. doi:10.1016/j.ijhydene.2018.01.099

56. Kaczur, J. J., Yang, H., Liu, Z., Sajjad, S. D., & Masel, R. I. (2018). Carbon Dioxide and Water Electrolysis Using New Alkaline Stable Anion Membranes. *Front Chem, 6*, 263. doi:10.3389/fchem.2018.00263

57. Kang, Q., Cao, J., Zhang, Y., Liu, L., Xu, H., & Ye, J. (2013). Reduced TiO2 nanotube arrays for photoelectrochemical water splitting. *Journal of Materials Chemistry A, 1*(18). doi:10.1039/c3ta10689f

58. Kang, X., Liu, S., Dai, Z., He, Y., Song, X., & Tan, Z. (2019). Titanium Dioxide: From Engineering to Applications. *Catalysts, 9*(2). doi:10.3390/catal9020191

59. Keating, C. (2020). Qatar utility hails ultra-low tariff in tender for 800MW bifacial PV park.

60. Kedzierzawski, P., & Augustynski, J. (1994). Poisoning and Activation of the Gold Cathode during Electroreduction of CO 2. *Journal of The Electrochemical Society, 141*(5), L58-L60. doi:10.1149/1.2054936

61. Kim, C., Kim, S., Choi, J., Lee, J., Kang, J. S., Sung, Y.-E., . . . Yoon, J. (2014). Blue TiO2 Nanotube Array as an Oxidant Generating Novel Anode Material Fabricated by Simple Cathodic Polarization. *Electrochimica Acta, 141*, 113-119. doi:10.1016/j.electacta.2014.07.062

62. Kim, H., Jeon, H. S., Jee, M. S., Nursanto, E. B., Singh, J. P., Chae, K., . . . Min, B. K. (2016). Contributors to Enhanced CO2 Electroreduction Activity and Stability in a Nanostructured Au Electrocatalyst. *ChemSusChem, 9*(16), 2097-2102. doi:https://doi.org/10.1002/cssc.201600228

63. Léger, J.-M., & Hahn, F. (2007). Chapter 3 - Contribution of In-situ Infrared Reflectance Spectroscopy in the Study of Nanostructured Fuel Cell Electrodes. In S.-G. Sun, P. A. Christensen, & A. Wieckowski (Eds.), *In-situ Spectroscopic Studies of Adsorption at the Electrode and Electrocatalysis* (pp. 63-98). Amsterdam: Elsevier Science B.V.

64. Li, H., Chen, Z., Tsang, C. K., Li, Z., Ran, X., Lee, C., . . . Li, Y. Y. (2014). Electrochemical doping of anatase TiO2in organic electrolytes for high-performance supercapacitors and photocatalysts. *J. Mater. Chem. A, 2*(1), 229-236. doi:10.1039/c3ta13963h

65. Li, R., & Li, C. (2017). Chapter One - Photocatalytic Water Splitting on Semiconductor-Based Photocatalysts. In C. Song (Ed.), *Advances in Catalysis* (Vol. 60, pp. 1-57): Academic Press.

66. Li, Z., Bian, H., Xu, Z., Lu, J., & Li, Y. Y. (2020). Solution-Based Comproportionation Reaction for Facile Synthesis of Black TiO2 Nanotubes and Nanoparticles. *ACS Applied Energy Materials*. doi:10.1021/acsaem.0c00976

67. Liang, S., He, J., Sun, Z., Liu, Q., Jiang, Y., Cheng, H., . . . Wei, S. (2012). Improving Photoelectrochemical Water Splitting Activity of TiO2 Nanotube Arrays by Tuning Geometrical Parameters. *The Journal of Physical Chemistry C, 116*(16), 9049-9053. doi:10.1021/jp300552s

68. Liu, X., Gao, S., Xu, H., Lou, Z., Wang, W., Huang, B., & Dai, Y. (2013). Green synthetic approach for Ti3+ self-doped TiO(2-x) nanoparticles with efficient visible light photocatalytic activity. *Nanoscale, 5*(5), 1870-1875. doi:10.1039/c2nr33563h

69. Luckow, P., A. Stanton, E., Fields, S., Biewald, B., Jackson, S., Fisher, J., & Wilson, R. (2015). 2015 Carbon Dioxide Price Forecast.

70. Luttrell, T., Halpegamage, S., Tao, J., Kramer, A., Sutter, E., & Batzill, M. (2014). Why is anatase a better photocatalyst than rutile?--Model studies on epitaxial TiO2 films. *Sci Rep, 4*, 4043. doi:10.1038/srep04043

71. Ma, Y., Wang, X., Jia, Y., Chen, X., Han, H., & Li, C. (2014). Titanium Dioxide-Based Nanomaterials for Photocatalytic Fuel Generations. *Chemical Reviews, 114*(19), 9987-10043. doi:10.1021/cr500008u

72. Maria, H., & Jin, L. (2001). Photoelectrochemical mineralization of textile diazo dye pollutants using nanocrystalline WO3 electrodes. *Electrochimica Acta*.

73. Martín, A. J., Larrazábal, G. O., & Pérez-Ramírez, J. (2015). Towards sustainable fuels and chemicals through the electrochemical reduction of CO2: lessons from water electrolysis. *Green Chemistry, 17*(12), 5114-5130. doi:10.1039/c5gc01893e

74. Masel, R. I., Liu, Z., Yang, H., Kaczur, J. J., Carrillo, D., Ren, S., . . . Berlinguette, C. P. (2021). An industrial perspective on catalysts for low-temperature CO2 electrolysis. *Nat Nanotechnol, 16*(2), 118-128. doi:10.1038/s41565-020-00823-x

75. Mohamed, M. A., Salleh, W. N. W., Jaafar, J., Ismail, A. F., & Nor, N. A. M. (2015). Photodegradation of phenol by N-Doped TiO2 anatase/rutile nanorods assembled microsphere under UV and visible light irradiation. *Materials Chemistry and Physics, 162*, 113-123. doi:https://doi.org/10.1016/j.matchemphys.2015.05.033

76. Nabil, S. K., McCoy, S., & Kibria, M. G. (2021). Comparative Life Cycle Assessment of Electrochemical Upgrading of CO2 to Fuels and Feedstocks. *Green Chemistry*. doi:10.1039/D0GC02831B

77. Naffati, N., Sampaio, M. J., Da Silva, E. S., Nsib, M. F., Arfaoui, Y., Houas, A., . . . Silva, C. G. (2020). Carbon-nanotube/TiO2 materials synthesized by a one-pot oxidation/hydrothermal route for the photocatalytic production of hydrogen from biomass derivatives. *Materials Science in Semiconductor Processing, 115*, 105098. doi:https://doi.org/10.1016/j.mssp.2020.105098

78. Naldoni, A., Allieta, M., Santangelo, S., Marelli, M., Fabbri, F., Cappelli, S., . . . Dal Santo, V. (2012). Effect of nature and location of defects on bandgap narrowing in black TiO2 nanoparticles. *J Am Chem Soc, 134*(18), 7600-7603. doi:10.1021/ja3012676

79. Naldoni, A., Altomare, M., Zoppellaro, G., Liu, N., Kment, S., Zboril, R., & Schmuki, P. (2019). Photocatalysis with Reduced TiO2: From Black TiO2 to Cocatalyst-Free Hydrogen Production. *ACS Catal, 9*(1), 345-364. doi:10.1021/acscatal.8b04068

80. Novelli, P. C. (1999). CO in the atmosphere: measurement techniques and related issues. *Chemosphere - Global Change Science, 1*(1), 115-126. doi:https://doi.org/10.1016/S1465-9972(99)00013-6
81. Ohring, M. (2002). Chapter 2 - Vacuum Science and Technology. In M. Ohring (Ed.), *Materials Science of Thin Films (Second Edition)* (pp. 57-93). San Diego: Academic Press.
82. Ojani, R., Raoof, J.-B., Khanmohammadi, A., & Zarei, E. (2012). Photoelectrocatalytic degradation of 3-nitrophenol at surface of Ti/TiO2 electrode. *Journal of Solid State Electrochemistry, 17*(1), 63-68. doi:10.1007/s10008-012-1853-x
83. Ola, O., & Maroto-Valer, M. M. (2015). Review of material design and reactor engineering on TiO2 photocatalysis for CO2 reduction. *Journal of Photochemistry and Photobiology C: Photochemistry Reviews, 24*, 16-42. doi:10.1016/j.jphotochemrev.2015.06.001
84. Ottmar, E., Ramon, P.-M., Youba, S., Ellie, F., Sussanne, K., Kristin, S., . . . Jan, C. M. (2014). *Climate Change 2014: Mitigation of Climate Change, Contribution of Working Group III to the Fifth Assessment Report of the Intergovernmental Panel on Climate Change* Retrieved from Cambridge, United Kingdom and New York, NY, USA:
85. Padmanabhan, N. T., Thomas, N., Louis, J., Mathew, D. T., Ganguly, P., John, H., & Pillai, S. C. (2021). Graphene coupled TiO2 photocatalysts for environmental applications: A review. *Chemosphere, 271*, 129506. doi:https://doi.org/10.1016/j.chemosphere.2020.129506
86. Pardal, T., Messias, S., Sousa, M., Machado, A. S. R., Rangel, C. M., Nunes, D., . . . da Ponte, M. N. (2017). Syngas production by electrochemical CO 2 reduction in an ionic liquid based-electrolyte. *Journal of CO2 Utilization, 18*, 62-72. doi:10.1016/j.jcou.2017.01.007
87. Paul, K. K., & Giri, P. K. (2018). Plasmonic Metal and Semiconductor Nanoparticle Decorated TiO2-Based Photocatalysts for Solar Light Driven Photocatalysis. In K. Wandelt (Ed.), *Encyclopedia of Interfacial Chemistry* (pp. 786-794). Oxford: Elsevier.
88. Ramdin, M., Morrison, A. R. T., de Groen, M., van Haperen, R., de Kler, R., van den Broeke, L. J. P., . . . Vlugt, T. J. H. (2019). High Pressure Electrochemical Reduction of CO2 to Formic Acid/Formate: A Comparison between Bipolar Membranes and Cation Exchange Membranes. *Industrial & Engineering Chemistry Research, 58*(5), 1834-1847. doi:10.1021/acs.iecr.8b04944
89. Ringe, S., Morales-Guio, C. G., Chen, L. D., Fields, M., Jaramillo, T. F., Hahn, C., & Chan, K. (2020). Double layer charging driven carbon dioxide adsorption limits the rate of electrochemical carbon dioxide reduction on Gold. *Nature Communications, 11*(1), 33. doi:10.1038/s41467-019-13777-z
90. Roy, P., Berger, S., & Schmuki, P. (2011). TiO2 nanotubes: synthesis and applications. *Angew Chem Int Ed Engl, 50*(13), 2904-2939. doi:10.1002/anie.201001374

91. Shah, U. H., Deen, K. M., Asgar, H., Rahman, Z., & Haider, W. (2017). Understanding the mechanism of TiO2 nanotubes formation at low potentials (≤ 8 V) through electrochemical methods. *Journal of Electroanalytical Chemistry, 807*, 228-234. doi:10.1016/j.jelechem.2017.11.014
92. Shen, S., Chen, J., Wang, M., Sheng, X., Chen, X., Feng, X., & Mao, S. S. (2018). Titanium dioxide nanostructures for photoelectrochemical applications. *Progress in Materials Science, 98*, 299-385. doi:10.1016/j.pmatsci.2018.07.006
93. Shin, H., Jeong, D.-K., Lee, J., Sung, M. M., & Kim, J. (2004). Formation of TiO2 and ZrO2 Nanotubes Using Atomic Layer Deposition with Ultraprecise Control of the Wall Thickness. *Advanced Materials, 16*(14), 1197-1200. doi:10.1002/adma.200306296
94. Sinhamahapatra, A., Jeon, J.-P., & Yu, J.-S. (2015). A new approach to prepare highly active and stable black titania for visible light-assisted hydrogen production. *Energy & Environmental Science, 8*(12), 3539-3544. doi:10.1039/c5ee02443a
95. Skoog, D. A., Holler, F. J., & Crouch, S. R. (2018). *Principles of instrumental analysis* (Seventh edition. ed.). Australia: Cengage Learning.
96. Smith, Y. R., Ray, R. S., Carlson, K., Sarma, B., & Misra, M. (2013). Self-Ordered Titanium Dioxide Nanotube Arrays: Anodic Synthesis and Their Photo/Electro-Catalytic Applications. *Materials (Basel), 6*(7), 2892-2957. doi:10.3390/ma6072892
97. Sun, Y., Wang, G., & Yan, K. (2011). TiO2 nanotubes for hydrogen generation by photocatalytic water splitting in a two-compartment photoelectrochemical cell. *International Journal of Hydrogen Energy, 36*(24), 15502-15508. doi:10.1016/j.ijhydene.2011.08.112
98. Sun, Z., Ma, T., Tao, H., Fan, Q., & Han, B. (2017). Fundamentals and Challenges of Electrochemical CO2 Reduction Using Two-Dimensional Materials. *Chem, 3*(4), 560-587. doi:https://doi.org/10.1016/j.chempr.2017.09.009
99. Tentu, R. D., & Basu, S. (2017). Photocatalytic water splitting for hydrogen production. *Current Opinion in Electrochemistry, 5*(1), 56-62. doi:10.1016/j.coelec.2017.10.019
100. Tho, N. T., Thi, C. M., Van Hieu, L., & Van Viet, P. (2019). Visible-light-driven photocatalysis for methylene blue degradation and hydrogen evolution reaction: a case of black TiO2 nanotube arrays. *Journal of the Australian Ceramic Society*. doi:10.1007/s41779-019-00405-8
101. Thorson, M. R., Siil, K. I., & Kenis, P. J. A. (2012). Effect of Cations on the Electrochemical Conversion of CO2to CO. *Journal of The Electrochemical Society, 160*(1), F69-F74. doi:10.1149/2.052301jes
102. Timo, K., & Nina, P. (2006). *Method Development of Gas Analysis with Mass Spectrometer*. Retrieved from https://inis.iaea.org/collection/NCLCollectionStore/_Public/43/061/43061183.pdf :

103. TOTAL. (2020). TOTAL TO DEVELOP QATAR’S FIRST LARGE-SCALE (800 MWP) SOLAR PLANT [Press release]

104. Ullattil, S. G., Narendranath, S. B., Pillai, S. C., & Periyat, P. (2018). Black TiO2 Nanomaterials: A Review of Recent Advances. *Chemical Engineering Journal, 343*, 708-736. doi:10.1016/j.cej.2018.01.069

105. Venturini, J., Bonatto, F., Guaglianoni, W. C., Lemes, T., Arcaro, S., Alves, A. K., & Bergmann, C. P. (2019). Cobalt-doped titanium oxide nanotubes grown via one-step anodization for water splitting applications. *Applied Surface Science, 464*, 351-359. doi:10.1016/j.apsusc.2018.09.093

106. Verma, S., Kim, B., Jhong, H. R., Ma, S., & Kenis, P. J. (2016). A Gross-Margin Model for Defining Technoeconomic Benchmarks in the Electroreduction of CO2. *ChemSusChem*, *9*(15), 1972-1979. doi:10.1002/cssc.201600394

107. Wang, B., Shen, S., & Mao, S. S. (2017). Black TiO 2 for solar hydrogen conversion. *Journal of Materiomics, 3*(2), 96-111. doi:10.1016/j.jmat.2017.02.001

108. Wang, H., Liu, Q., & You, C. (2019). Regeneration of sulfur-deactivated TiO2 photocatalysts. *Applied Catalysis A: General, 572*, 15-23. doi:https://doi.org/10.1016/j.apcata.2018.12.031

109. Wang, Z., Yang, C., Lin, T., Yin, H., Chen, P., Wan, D., . . . Jiang, M. (2013a). H-Doped Black Titania with Very High Solar Absorption and Excellent Photocatalysis Enhanced by Localized Surface Plasmon Resonance. *Advanced Functional Materials, 23*(43), 5444-5450. doi:10.1002/adfm.201300486

110. Wang, Z., Yang, C., Lin, T., Yin, H., Chen, P., Wan, D., . . . Jiang, M. (2013b). Visible-light photocatalytic, solar thermal and photoelectrochemical properties of aluminium-reduced black titania. *Energy & Environmental Science, 6*(10). doi:10.1039/c3ee41817k

111. Westbroek, P. (2005). 2 - Electrochemical methods. In P. Westbroek, G. Priniotakis, & P. Kiekens (Eds.), *Analytical Electrochemistry in Textiles* (pp. 37-69): Woodhead Publishing.

112. White, J. L., Baruch, M. F., Pander Iii, J. E., Hu, Y., Fortmeyer, I. C., Park, J. E., . . . Bocarsly, A. B. (2015). Light-Driven Heterogeneous Reduction of Carbon Dioxide: Photocatalysts and Photoelectrodes. *Chem Rev, 115*(23), 12888-12935. doi:10.1021/acs.chemrev.5b00370

113. Wu, H., Li, D., Zhu, X., Yang, C., Liu, D., Chen, X., . . . Lu, L. (2014). High-performance and renewable supercapacitors based on TiO2 nanotube array electrodes treated by an electrochemical doping approach. *Electrochimica Acta, 116*, 129-136. doi:10.1016/j.electacta.2013.10.092

114. Wuttig, A., Yaguchi, M., Motobayashi, K., Osawa, M., & Surendranath, Y. (2016). Inhibited proton transfer enhances Au-catalyzed CO<sub>2</sub>-to-fuels selectivity. *Proceedings of the National Academy of Sciences, 113*(32), E4585. doi:10.1073/pnas.1602984113

115. Xiaobo, C., Lei, L., Peter, Y. Y., & Samuel, S. M. (2011). Increasing Solar Absorption for Photocatalysis with Black Hydrogenated Titanium Dioxide Nanocrystals. *Science*.

116. Xu, C., Li, M., Ji, X., & Chen, F. (2013, 19-21 Aug. 2013). *Study on the collection efficiency of parabolic trough solar collector.* Paper presented at the 2013 International Conference on Materials for Renewable Energy and Environment.

117. Xu, G., Feng, Q., Wang, Z., Lv, J., Huang, J., Li, Y., . . . Wu, Y. (2019). Structures and photoelectrochemical performances of reduced TiO2 NTAs obtained by hydrogen thermal and electrochemical reduction methods. *Journal of Solid State Electrochemistry, 24*(2), 365-374. doi:10.1007/s10008-019-04358-7

118. Xu, X., Cai, J., Zhou, M., Du, X., & Zhang, Y. (2020). Photoelectrochemical degradation of 2,4-dichlorophenoxyacetic acid using electrochemically self-doped Blue TiO2 nanotube arrays with formic acid as electrolyte. *J Hazard Mater, 382*, 121096. doi:10.1016/j.jhazmat.2019.121096

119. Xuemei Zhou, N. L., and Patrik Schmuki. (2017). Photocatalysis with TiO2 Nanotubes: “Colorful” Reactivity and Designing Site-Specific Photocatalytic Centers into TiO2 Nanotubes. *ACS Catalysis*. doi:10.1021/acscatal.6b03709

120. Yan, P., Liu, G., Ding, C., Han, H., Shi, J., Gan, Y., & Li, C. (2015). Photoelectrochemical water splitting promoted with a disordered surface layer created by electrochemical reduction. *ACS Appl Mater Interfaces, 7*(6), 3791-3796. doi:10.1021/am508738d

121. Yan, X., Li, Y., & Xia, T. (2017). Black Titanium Dioxide Nanomaterials in Photocatalysis. *International Journal of Photoenergy, 2017,* 1-16. doi:10.1155/2017/8529851

122. Yao, T., An, X., Han, H., Chen, J. Q., & Li, C. (2018). Photoelectrocatalytic Materials for Solar Water Splitting. *Advanced Energy Materials, 8*(21). doi:10.1002/aenm.201800210

123. Yu, L., Li, M., Huang, C., Zhang, Y., He, J., Zhou, X., & Zhu, H. (2018). Photoelectrochemical properties of N doped black TiO 2 nanotube arrays. *Materials Letters, 216*, 239-242. doi:10.1016/j.matlet.2018.01.126

124. Zhang, G., Zhang, W., Minakata, D., Chen, Y., Crittenden, J., & Wang, P. (2013). The pH effects on H2 evolution kinetics for visible light water splitting over the Ru/(CuAg)0.15In0.3Zn1.4S2 photocatalyst. *International Journal of Hydrogen Energy, 38*(27), 11727-11736. doi:https://doi.org/10.1016/j.ijhydene.2013.06.140

125. Zhang, M., Bando, Y., & Wada, K. (2001). Sol-Gel Template Preparation of TiO2 nanotubes and nanorods. *Journal of Materials Science Letters, 20,* 167-170. doi:10.1023/A:1006739713220

126. Zhang, Z., Hedhili, M. N., Zhu, H., & Wang, P. (2013). Electrochemical reduction induced self-doping of Ti3+ for efficient water splitting performance on TiO2 based photoelectrodes. *Phys Chem Chem Phys, 15*(37), 15637-15644. doi:10.1039/c3cp52759j

127. Zhao, J., Xue, S., Barber, J., Zhou, Y., Meng, J., & Ke, X. (2020). An overview of Cu-based heterogeneous electrocatalysts for CO2 reduction. *Journal of Materials Chemistry A, 8*(9), 4700-4734. doi:10.1039/c9ta11778d

128. Zhao, Z., Tan, H., Zhao, H., Lv, Y., Zhou, L. J., Song, Y., & Sun, Z. (2014). Reduced TiO2 rutile nanorods with well-defined facets and their visible-light photocatalytic activity. *Chem Commun (Camb), 50*(21), 2755-2757. doi:10.1039/c3cc49182j

129. Zheng, Q., Lee, H.-J., Lee, J., Choi, W., Park, N.-B., & Lee, C. (2014). Electrochromic titania nanotube arrays for the enhanced photocatalytic degradation of phenol and pharmaceutical compounds. *Chemical Engineering Journal, 249*, 285-292. doi:10.1016/j.cej.2014.03.111

130. Zhou, H., & Zhang, Y. (2014). Electrochemically Self-Doped TiO2 Nanotube Arrays for Supercapacitors. *The Journal of Physical Chemistry C, 118*(11), 5626-5636. doi:10.1021/jp4082883

131. Zhu, L., Ma, H., Han, H., Fu, Y., Ma, C., Yu, Z., & Dong, X. (2018). Black TiO2 nanotube arrays fabricated by electrochemical self-doping and their photoelectrochemical performance. *RSC Advances, 8*(34), 18992-19000. doi:10.1039/c8ra02983k

APPENDIX A

OPTIMIZATION OF TIO$_2$ NANOTUBE

A.1. Optimization of white TiO$_2$ nanotubular structure

This section shows the changes in morphology with pretreatment methods and anodization conditions. The titanium sheet was either used as it is, polished by sandpaper, or etched by oxalic acid. Then, the sheet was further cleaned with ultrasonication. We varied the anodization conditions for the electrical voltage 30 and 50V and in a time interval of 1 to 5h. Then, surface characterization was used to investigate the resulting morphology. Figure 30 shows SEM results for surface morphology of the samples obtained at four different conditions. In Figure 30a, at 30V and 3h, nanodots' formation is observed. A mixture of nanotubes and nanorods was formed at 50V (as shown in Figure 30c and 33d) suggesting that the transformation to a nanotube structure requires longer than three hours to evolve to nanotubes. Titanium sheet cleaned only by ultrasonication produced a uniform nanotube structure when anodized at 30V for 5h, as shown in Figure 30b.

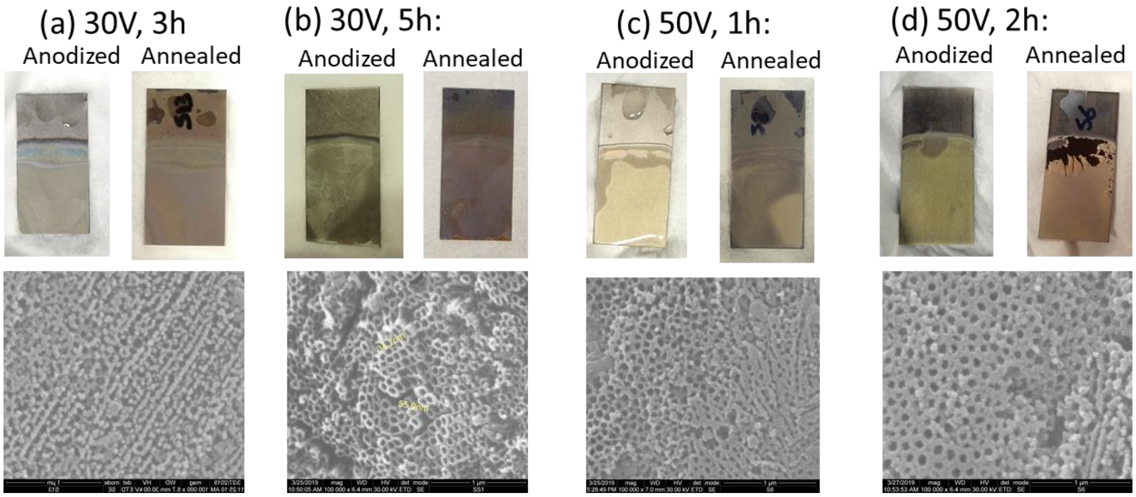

Figure 30. Surface morphology of the samples at different conditions: (a) and (c) are pretreated by chemical etching with oxalic acid followed by ultrasonication (b) only ultrasonication, and (d) with sandpaper followed by ultrasonication.

A.2. The effect of annealing temperature variation

In this section, several samples were prepared at the same anodization conditions while changing the annealing temperature from 300 to 600˚C. Then the samples were electrochemically reduced before characterization using SEM and XRD. The visual observation of the effect of annealing that the color of the samples ranges from light brown to bluish-grey as the temperature was increased. The SEM shows a nanotubular morphology for the different samples and around the same pore diameter. However, in the XRD, there is a phase change at 600˚C, where the rutile phase starts to appear. The characteristic peak at 25.5˚ is attributed to anatase crystalline phase and it is the sharpest at 400˚C. Therefore, this temperature was chosen as the optimized temperature for uniform anatase phase(Mohamed et al., 2015).

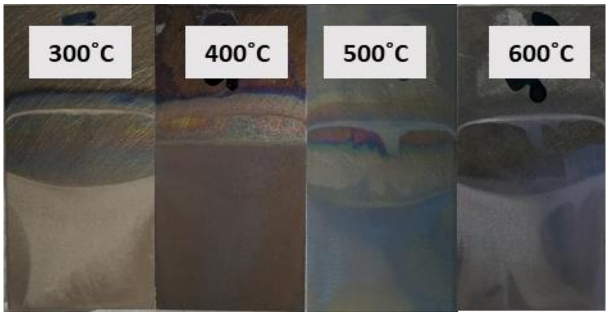

Figure 31: TNT samples after annealing

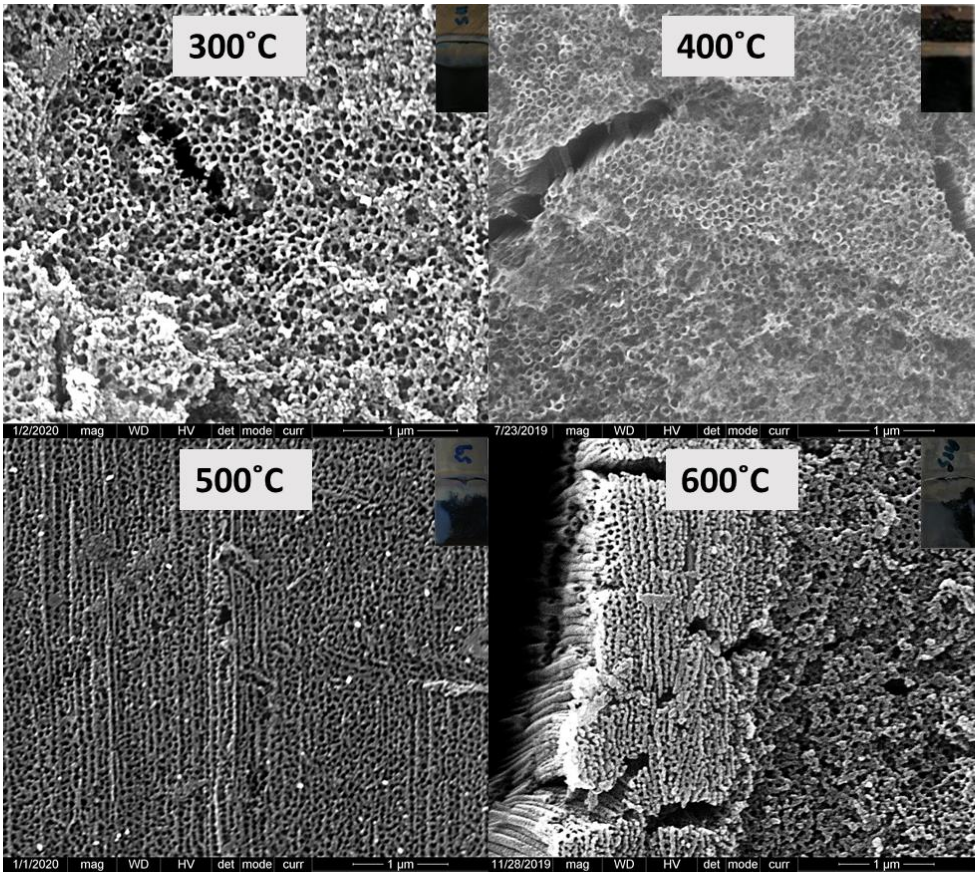

Figure 32: SEM to show the morphology of BTNT where the inset represents the characterized sample

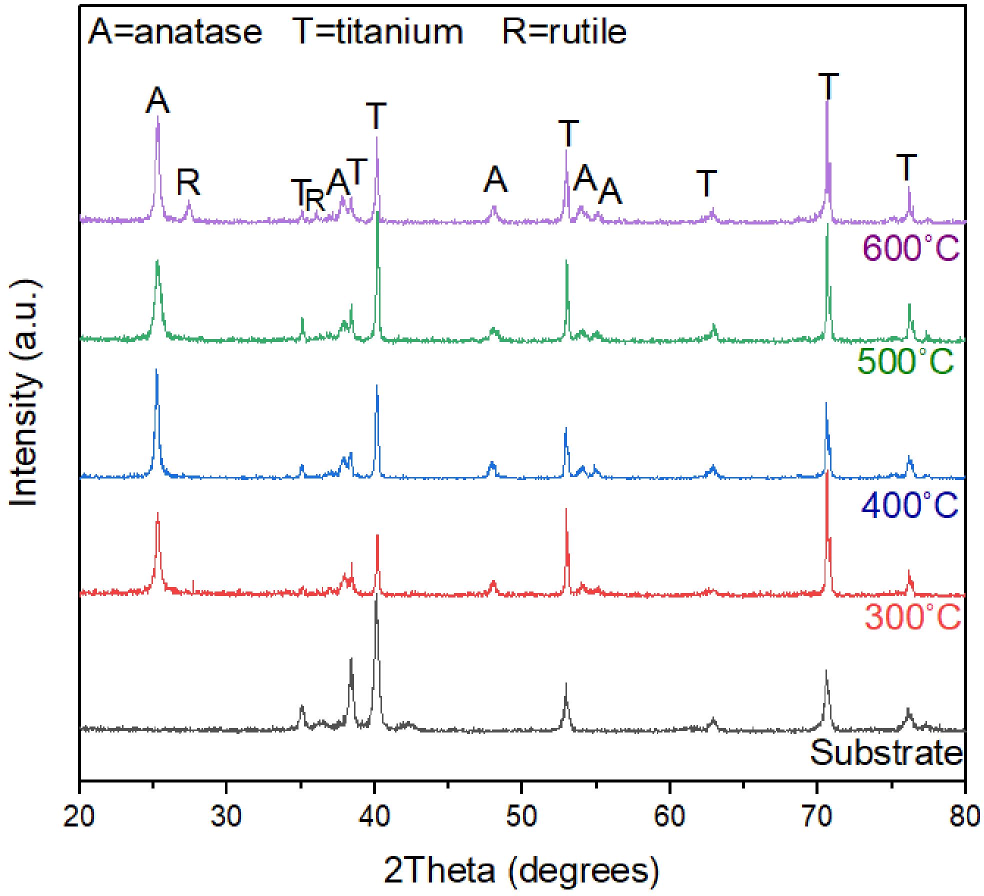

Figure 33: XRD patterns for BTNTs at different temperatures

APPENDIX B

DETAILED SUSTAINABILITY CALCULATIONS

B.1. Assumptions

1. CO_2 stream is purified from flue gas consisting of 3vol% CO_2 from a natural gas midstream facility (Afzal et al., 2018).
2. For the experimental setup, an overpotential of 0.3V for the anode reaction was assumed then the cell potential was calculated and used for the EE%.
3. The conversion percentage in the literature reported systems is needed for calculating the CO_2 amount. It is usually not reported; thus, it was calculated as follows:

$$X\% = \frac{FE\%_{(CO)} \times CO_{(max)}}{CO_{2_{in}}} \ldots\ldots\ldots\ldots\ldots\ldots\ldots\ldots\ldots\ldots\ldots\ldots [B\text{- }1]$$

Where, the maximum CO is obtained from faraday's law of electrolysis:

$$CO_{(max)}\left(\frac{mol}{s}\right) = \frac{jA \times 10^{-3}}{nF} \ldots\ldots\ldots\ldots\ldots\ldots\ldots\ldots\ldots\ldots\ldots [B\text{- }2]$$

4. The conversion in the experimental setup was calculated from detected H_2 and the maximum dissolved CO_2. The dissolved amount was calculated from the solubility (30mM in the water at 25C and 1atm) (Martín et al., 2015).
5. The operating cost includes the costs of electricity, the balance of plant, and raw material costs (i.e., CO_2 gas).
6. The balance of the plant is taken to be 10% of the electricity costs (Adnan et al., 2020).

B.2. Calculations steps

1. Reactions in the system:

	Reaction	**Equilibrium potential (V)**
At the anode	$2H_2O \rightarrow O_2 + 4H^+ + 4e^-$	1.23
At the cathode	$CO_2 + 2H^+ + 2e^- \rightarrow CO + H_2O$	-0.103
	$2H^+ + 2e^- \rightarrow H_2$	0
Overall	$CO_2 + H_2O \rightarrow CO + O_2 + H_2$	-1.333

For the overall reaction, the equilibrium potential is calculated by (Ciobanu et al., 2007)

$$\Delta E^{\circ} = E_{cathode}^{\circ} - E_{anode}^{\circ} \ldots\ldots\ldots\ldots\ldots\ldots\ldots\ldots\ldots\ldots\ldots [B\text{- }3]$$

2. The area of the electrolyzer based on the production target can be calculated:

$$A = \frac{N \times n \times F}{j} \ldots\ldots\ldots\ldots\ldots\ldots\ldots\ldots\ldots\ldots\ldots\ldots [B\text{- }4]$$

Where N= total syngas flowrate (mol/s)

3. The CO number of moles were calculated from stoichiometry (1:1) and the conversion:

$$N_{CO_2} = \frac{N_{CO}}{X\%} \ldots\ldots\ldots\ldots\ldots\ldots\ldots\ldots\ldots\ldots\ldots\ldots [B\text{- }5]$$

4. The total energy requirement is divided by the energy efficiency (EE%) of the electrolysis as follows:

$$E = \frac{1.1 \times V \times J \times A \times t}{EE\%} \ldots\ldots\ldots\ldots\ldots\ldots\ldots\ldots\ldots\ldots [B\text{- }6]$$

The formula is multiplied by 10% to account for the balance of the plant.

5. Subsequently, the emissions are calculated by multiplying the amount of electricity with the factor as reported in
6. Table 3:

$$CO_2\ footprint\ of\ PV\ panels = Electricity(kWh) \times factor\ (gCO_2/kWh)$$

7. The emissions from the CO_2 source are obtained using the factor in
8. Table 3 as follows:

$$CO_2\ emissions\ from\ CO_2\ source = \ amount\ of\ CO_2\ (kg) \times factor\ (gCO_2/kgCO_2)$$

9. $The\ consumed\ CO_2\ is = X \times N_{CO2} \times\ Mw\ (g/mol).$
10. Finally,

$$The\ total\ emissions = \ CO_2\ emissions\ from\ (PV\ utility + \ CO_2\ source)\ -\ consumed\ CO_2$$

11. The electricity and raw material costs are directly obtained by multiplying the amounts into the price from
12. Table **3**.
13. The below parameters were calculated from the specifications of each experiment and used in the above calculations.

Calculated parameters	**Experimental setup**	**Siemens**	**Dioxide Materials**
EE%	60%	37%	45%
X%	0.2%	30%	20%
Ratio H_2:CO	1.00	1.12	0.02
Syngas kmol/day	71.43	75.83	71.43